COORDINATED MULTIWAVELENGTH OBSERVATION OF 3C 66A DURING THE WEBT CAMPAIGN OF 2003–2004[1]

M. BÖTTCHER,[2] J. HARVEY,[2] M. JOSHI,[2] M. VILLATA,[3] C. M. RAITERI,[3] D. BRAMEL,[4] R. MUKHERJEE,[4] T. SAVOLAINEN,[5]
W. CUI,[6] G. FOSSATI,[7] I. A. SMITH,[7] D. ABLE,[6] H. D. ALLER,[8] M. F. ALLER,[8] A. A. ARKHAROV,[9] T. AUGUSTEIJN,[10]
K. BALIYAN,[11] D. BARNABY,[12] A. BERDYUGIN,[5] E. BENÍTEZ,[13] P. BOLTWOOD,[14] M. CARINI,[12] D. CAROSATI,[15]
S. CIPRINI,[16] J. M. COLOMA,[17] S. CRAPANZANO,[3] J. A. DE DIEGO,[13] A. DI PAOLA,[18] M. DOLCI,[19] J. FAN,[20]
A. FRASCA,[21] V. HAGEN-THORN,[22,23] D. HORAN,[24] M. IBRAHIMOV,[25,26] G. N. KIMERIDZE,[27] Y. A. KOVALEV,[28]
Y. Y. KOVALEV,[28,29] O. KURTANIDZE,[27] A. LÄHTEENMÄKI,[30] L. LANTERI,[3] V. M. LARIONOV,[22,23]
E. G. LARIONOVA,[22] E. LINDFORS,[5] E. MARILLI,[21] N. MIRABAL,[31] M. NIKOLASHVILI,[27]
K. NILSSON,[5] J. M. OHLERT,[32] T. OHNISHI,[33] A. OKSANEN,[34] L. OSTORERO,[5,35]
G. OYER,[10] I. PAPADAKIS,[36,37] M. PASANEN,[5] C. POTEET,[12] T. PURSIMO,[10]
K. SADAKANE,[33] L. A. SIGUA,[27] L. TAKALO,[5] J. B. TARTAR,[38]
H. TERÄSRANTA,[30] G. TOSTI,[16] R. WALTERS,[12] K. WIIK,[5,39]
B. A. WILKING,[38] W. WILLS,[12] E. XILOURIS,[40]
A. B. FLETCHER,[41] M. GU,[41,42,43] C.-U. LEE,[32]
S. PAK,[41] AND H.-S. YIM[41]

ABSTRACT

The BL Lac object 3C 66A was the target of an extensive multiwavelength monitoring campaign from 2003 July through 2004 April (with a core campaign from 2003 September to 2003 December) involving observations throughout the electromagnetic spectrum. Radio, infrared, and optical observations were carried out by the WEBT-ENIGMA collaboration. At higher energies, 3C 66A was observed in X-rays (*RXTE*), and at very high energy (VHE) in γ-rays (STACEE, VERITAS). In addition, the source has been observed with the VLBA at nine epochs throughout the period 2003 September to 2004 December, including three epochs contemporaneous with the core campaign. A gradual brightening of the source over the course of the campaign was observed at all optical frequencies, culminating in a very bright maximum around 2004 February 18. The WEBT campaign revealed microvariability with flux changes of $\sim$5% on timescales as short as $\sim$2 hr. The source was in a relatively bright state, with several bright flares on timescales of several days. The spectral energy distribution (SED) indicates a νF_ν peak in the optical regime. A weak trend of optical spectral hysteresis with a trend of spectral softening throughout both the rising and decaying phases has been found. On longer timescales, there appears to be a weak indication of a positive hardness-intensity correlation for low optical fluxes, which does not persist at higher flux levels. The 3–10 keV X-ray flux of 3C 66A during the core campaign was historically high and its spectrum very soft, indicating that the low-frequency component of the broadband SED extends beyond $\sim$10 keV. No significant X-ray flux and/or spectral variability was detected. STACEE and Whipple observations provided upper flux limits at >150 and >390 GeV, respectively. The 22 and 43 GHz data from the three VLBA epochs made between 2003 September and 2004 January indicate a rather smooth jet with only very moderate internal structure. Evidence for superluminal motion ($8.5 \pm 5.6\ h^{-1}\ c$) was found in only one of six components, while the apparent velocities of all other components are consistent with 0. The radial radio brightness profile suggests a magnetic field decay $\propto r^{-1}$ and, thus, a predominantly perpendicular magnetic field orientation.

Subject headings: BL Lacertae objects: individual (3C 66A) — galaxies: active — gamma rays: theory — radiation mechanisms: nonthermal

Online material: color figure

[1] For questions regarding the availability of the data from the WEBT (Whole Earth Blazar Telescope) campaign presented in this paper, please contact the WEBT president Massimo Villata at villata@to.astro.it.
[2] Astrophysical Institute, Department of Physics and Astronomy, Clippinger 339, Ohio University, Athens, OH 45701.
[3] Istituto Nazionale di Astrofisica (INAF), Osservatorio Astronomico di Torino, Via Osservatorio 20, I-10025 Pino Torinese, Italy.
[4] Barnard College, Columbia University, New York, NY 10027.
[5] Tuorla Observatory, University of Turku, 21500 Piikkiö, Finland.
[6] Department of Physics, Purdue University, 525 Northwestern Avenue, West Lafayette, IN 47907-1396.
[7] Department of Physics and Astronomy, Rice University, MS 108, 6100 South Main Street, Houston, TX 77005-1892.
[8] Department of Astronomy, University of Michigan, 830 Dennison Building, Ann Arbor, MI 48109-1090.
[9] Pulkovo Observatory, Pulkovskoye Shosse, 65, 196140 St. Petersburg, Russia.
[10] Nordic Optical Telescope, Apartado 474, E-38700 Santa Cruz de La Palma, Santa Cruz de Tenerife, Spain.
[11] Physical Research Laboratory, Ahmedabad 3800 009, India.
[12] Department of Physics and Astronomy, Western Kentucky University, 1 Big Red Way, Bowling Green, KY 42104.
[13] Instituto de Astronomía, UNAM, Apartado Postal 70-264, 04510 México DF, Mexico.
[14] Boltwood Observatory, 1655 Stittsville Main Street, Stittsville, ON K2S 1N6, Canada.
[15] Osservatorio di Armenzano, Assisi, Italy.
[16] Osservatorio Astronomico, Università di Perugia, Via B. Bonfigli, I-06126 Perugia, Italy.
[17] Agrupaciòn Astronomica de Sabadell, Sabadell 08200, Spain.

1. INTRODUCTION

BL Lac objects and flat-spectrum radio quasars (FSRQs) are active galactic nuclei (AGNs) commonly unified in the class of blazars. They exhibit some of the most violent high-energy phenomena observed in AGNs to date. They are characterized by nonthermal continuum spectra, a high degree of linear polarization in the optical, rapid variability at all wavelengths, radio jets with individual components often exhibiting apparent superluminal motion, and—at least episodically—a significant portion of the bolometric flux emitted in γ-rays. Forty-six blazars have been detected and identified with high confidence in high-energy (>100 MeV) γ-rays by the EGRET instrument on board the *Compton Gamma Ray Observatory* (Hartman et al. 1999; Mattox et al. 2001). The properties of BL Lac objects and blazar-type FSRQs are generally very similar, except that BL Lac objects usually show only weak emission or absorption lines (with equivalent width in the rest-frame of the host galaxy of <5 Å), if any. In 3C 66A (=0219+428 = NRAO 102 = 4C 42.07), a weak Mg II emission line has been detected by Miller et al. (1978). This led to the determination of its redshift at $z = 0.444$, which was later confirmed by the detection of a weak Lyα line in the *International Ultraviolet Explorer* spectrum of 3C 66A (Lanzetta et al. 1993). However, as recently pointed out by Bramel et al. (2005), these redshift determinations are actually still quite uncertain. In this paper we do base our analysis on a redshift value of $z = 0.444$, but we remind the reader that some results of the physical interpretation should be considered as tentative pending a more solid redshift determination.

In the framework of relativistic jet models, the low-frequency (radio–optical/UV) emission from blazars is interpreted as synchrotron emission from nonthermal electrons in a relativistic jet. The high-frequency (X-ray to γ-ray) emission could be produced either via Compton upscattering of low-frequency radiation by the same electrons responsible for the synchrotron emission (leptonic jet models; for a recent review, see, e.g., Böttcher 2002), or by hadronic processes initiated by relativistic protons co-accelerated with the electrons (hadronic models; for a recent discussion, see, e.g., Mücke & Protheroe 2001; Mücke et al. 2003).

To date, six blazars have been detected at very high energies (>300 GeV) with ground-based air Cerenkov detectors (Punch et al. 1992; Quinn et al. 1996; Catanese et al. 1998; Chadwick et al. 1999; Aharonian et al. 2002; Horan et al. 2002; Holder et al. 2003). All of these belong to the subclass of high-frequency peaked BL Lac objects (HBLs). The field of extragalactic GeV–TeV astronomy is currently one of the most exciting research areas in astrophysics, as the steadily improving flux sensitivities of the new generation of air Cerenkov telescope arrays and their decreasing energy thresholds (for a recent review see, e.g., Weekes et al. 2002) provide a growing potential to extend their extragalactic source list toward intermediate- and even low-frequency peaked BL Lac objects (LBLs) with lower νF_ν peak frequencies in their broadband spectral energy distributions (SEDs). Detection of such objects at energies $\sim$40–100 GeV might provide an opportunity to probe the intrinsic high-energy cutoff of their SEDs since at those energies, $\gamma\gamma$ absorption due to the intergalactic infrared background is still expected to be small (e.g., de Jager & Stecker 2002).

3C 66A has been suggested as a promising candidate for detection by the new generation of atmospheric Cerenkov telescope facilities such as STACEE (Solar Tower Air Cerenkov Effect Experiment) or VERITAS (Very Energetic Radiation Imaging Telescope Array System; e.g., Costamante & Ghisellini 2002). Neshpor et al. (1998, 2000) have actually reported multiple detections of the source with the GT-48 telescope of the Crimean Astrophysical Observatory, but those have not been confirmed by any other group so far (see, e.g., Horan et al. 2004).

3C 66A is classified as a low-frequency peaked BL Lac object (LBL), a class also commonly referred to as radio-selected BL Lac objects. Its low-frequency spectral component typically peaks at IR–UV wavelengths, while the high-frequency component seems to peak in the multi-MeV–GeV energy range. Since its optical identification by Wills & Wills (1974), 3C 66A has been the target of many radio, IR, optical, X-ray, and γ-ray observations, although it is not as regularly monitored at radio frequencies as many other blazars due to problems with source confusion with the nearby radio galaxy 3C 66B (6$.\!'$5 from 3C 66A), in particular at lower (4.8 and 8 GHz) frequencies (Aller et al. 1994; Takalo et al. 1996).

[18] Istituto Nazionale di Astrofisica (INAF), Osservatorio Astronomico di Roma, Via Frascati, Monteporzio Cantone, Rome, Italy.
[19] Istituto Nazionale di Astrofisica (INAF), Osservatorio Astronomico di Teramo, Via Maggini, Teramo, Italy.
[20] Center for Astrophysics, Guangzhou University, Guangzhou 510400, China.
[21] Osservatorio Astrofisico di Catania, Viale A. Doria 6, I-95125 Catania, Italy.
[22] Astronomical Institute, St. Petersburg State University, Universitetsky pr. 28, Petrodvoretz, 198504 St. Petersburg, Russia.
[23] Isaac Newton Institute of Chile, St. Petersburg Branch, 198504 St. Petersburg, Russia.
[24] Harvard-Smithsonian Astrophysical Observatory, 60 Garden Street, Cambridge, MA 02138.
[25] Ulugh Beg Astronomical Institute, Academy of Sciences of Uzbekistan, 33 Astronomical Street, Tashkent 700052, Uzbekistan.
[26] Isaac Newton Institute of Chile, Uzbekistan Branch.
[27] Abastumani Observatory, 383762 Abastumani, Georgia.
[28] Astro Space Center, Profsoyuznaya Steet 5 84/32, Moscow 117997, Russia.
[29] National Radio Astronomy Observatory, P.O. Box 2, Green Bank, WV 24944; Jansky Fellow.
[30] Metsähovi Radio Observatory, Helsinki University of Technology, Metsähovintie 114, 02540 Kylmälä, Finland.
[31] Department of Physics and Astronomy, Columbia University, New York, NY 10027.
[32] Michael Adrian Observatory, Astronomie-Stiftung Trebur, Fichtenstrasse 7, D-65468 Trebur, Germany.
[33] Astronomical Institute, Osaka Kyoiku University, Kashiwara-shi, Osaka 582-8582, Japan.
[34] Nyrölä Observatory, Jyväskylän Sirius ry, Kyllikinkatu 1, 40950 Jyväskylä, Finland.
[35] Landessternwarte Heidelberg-Königstuhl, Königstuhl, D-69117 Heidelberg, Germany.
[36] Physics Department, University of Crete, GR 71003 Heraklion, Crete, Greece.
[37] IESL, Foundation for Research and Technology-Hellas, GR 71110 Heraklion, Crete, Greece.
[38] Department of Physics and Astronomy, University of Missouri, 8001 Natural Bridge Road, St. Louis, MO 63121.
[39] Institute of Space and Astronautical Science, Japan Aerospace Exploration Agency, 3-1-1 Yoshinodai, Sagamihara, Kanagawa 229-8510, Japan.
[40] Institute of Astronomy and Astrophysics, NOA, I. Metaxa anf Vas. Pavlou str., Palaia Penteli, Athens, Greece.
[41] Korea Astronomy and Space Science Institute, 61-1 Whaam-Dong, Yuseong-Gu, Daejeon 305-348, South Korea.
[42] Shanghai Astronomical Observatory, Chinese Academy of Sciences, 80 Nandan Road, Shanghai 200030, China.
[43] National Astronomical Observatories, Chinese Academy of Sciences, Beijing 100012, China.

The long-term variability of 3C 66A at near-IR (*J*, *H*, and *K* bands) and optical (*UBVRI*) wavelengths has recently been compiled and analyzed by Fan & Lin (1999 and 2000, respectively). Variability at those wavelengths is typically characterized by variations over ≲1.5 mag on timescales ranging from ∼1 week to several years. A positive correlation between the $B - R$ color (spectral hardness) and the *R* magnitude has been found by Vagnetti et al. (2003). An intensive monitoring effort by Takalo et al. (1996) revealed evidence for rapid microvariability, including a decline ∼0.2 mag within ∼6 hr. Microvariability had previously been detected in 3C 66A by Carini & Miller (1991) and De Diego et al. (1997), while other, similar efforts did not reveal such evidence (e.g., Miller & McGimsey 1978; Takalo et al. 1992; Xie et al. 1992). Lainela et al. (1999) also report on a 65 day periodicity of the source in its optically bright state, which has so far not been confirmed in any other analysis.

3C 66A is generally observed as a point source, with no indication of the host galaxy. The host galaxy of 3C 66A was marginally resolved by Wurtz et al. (1996). They found $R_{\rm Gunn} = 19.0$ mag for the host galaxy; the Hubble type could not be determined.

In X-rays, the source has been previously detected by *EXOSAT* (*European X-Ray Observatory Satellite*; Sambruna et al. 1994), *Einstein* (Worrall & Wilkes 1990), *ROSAT* (*Röntgensatellit*; Fossati et al. 1998), *BeppoSAX* (Perri et al. 2003), and *XMM-Newton* (Croston et al. 2003). It shows large-amplitude soft X-ray variability among these various epochs of observation, with flux levels at 1 keV ranging from ∼0.4 to ∼5 μJy and generally steep (energy index $\alpha > 1$) soft X-ray spectra below 1 keV. 3C 66A has also been detected in >100 MeV γ-rays by EGRET on several occasions, with flux levels up to $F_{>100\,{\rm MeV}} = (25.3 \pm 5.8) \times 10^{-8}$ photons cm^{-2} s^{-1} (Hartman et al. 1999).

Superluminal motion of individual radio components of the jet has been detected by Jorstad et al. (2001). While the identification of radio knots across different observing epochs is not unique, Jorstad et al. (2001) favor an interpretation implying superluminal motions of up to $\beta_{\rm app} \sim 19\ h^{-1} \approx 27$. This would imply a lower limit on the bulk Lorentz factor of the radio-emitting regions of $\Gamma \geq 27$. However, theoretical modeling of the nonsimultaneous SED of 3C 66A (Ghisellini et al. 1998) suggests a bulk Lorentz factor of the emitting region close to the core—where the γ-ray emission is commonly believed to be produced—of $\Gamma \sim 14$, more typical of the values obtained for other blazars as well.

In spite of the considerable amount of observational effort spent on 3C 66A (see, e.g., Takalo et al. 1996 for an intensive optical monitoring campaign on this source), its multiwavelength SED and correlated broadband spectral variability behavior are still surprisingly poorly understood, given its possible VHE γ-ray source candidacy. The object has never been studied in a dedicated multiwavelength campaign during the lifetime of EGRET. There have been few attempts of coordinated multiwavelength observations. For example, Worrall et al. (1984) present quasi-simultaneous radio, IR, optical, and UV observations of 3C 66A in 1983, but observations at different wavelength bands were still separated by up to ∼2 weeks, and no simultaneous higher energy data were available. This is clearly inadequate to seriously constrain realistic, physical emission models, given the established large-amplitude variability on similar timescales and the importance of the high-energy emission in the broadband SED of the source.

For this reason, we organized an intensive multiwavelength campaign to observe 3C 66A from 2003 July through 2004 April,

focusing on a core campaign from 2003 September to 2003 December. In § 2 we describe the observations and data analysis and present light curves in the various frequency bands. Spectral variability patterns are discussed in § 3, and the results of our search for interband cross-correlations and time lags are presented in § 4. Simultaneous broadband SEDs of 3C 66A at various optical brightness levels are presented in § 5. In § 6 we use our results to derive estimates of physical parameters, independent of the details of any specific model. We summarize in § 7. In a companion paper (M. Joshi & M. Böttcher 2005, in preparation), we will use time-dependent leptonic models to fit the spectra and variability patterns found in this campaign and make specific predictions concerning potentially observable X-ray spectral variability patterns and γ-ray emission.

Throughout this paper we refer to α as the energy spectral index, $F_\nu({\rm Jy}) \propto \nu^{-\alpha}$. A cosmology with $\Omega_m = 0.3$, $\Omega_\Lambda = 0.7$, and $H_0 = 70$ km s^{-1} Mpc^{-1} is used. In this cosmology, and using the redshift of $z = 0.444$, the luminosity distance of 3C 66A is $d_L = 2.46$ Gpc.

2. OBSERVATIONS, DATA REDUCTION, AND LIGHT CURVES

3C 66A was observed in a coordinated multiwavelength campaign at radio, near-IR, optical (by the WEBT-ENIGMA collaboration), X-ray, and VHE γ-ray energies during a core campaign period from 2003 September to 2003 December. The object is being continuously monitored at radio and optical wavelength by several ongoing projects, and we present data in those wavelengths regimes starting in 2003 July. During the core campaign, we found that the source was gradually brightening, indicating increasing activity throughout the campaign period. For this reason, the WEBT campaign was extended, and we continued to achieve good time coverage until early 2004 March, and individual observatories still contributed data through 2004 April. The overall time line of the campaign, along with the measured long-term light curves at radio, infrared, optical, and X-ray frequencies, is illustrated in Figure 1. Table 1 lists all participating observatories that contributed data to this campaign. In this section we will describe the individual observations in the various frequency ranges and outline the data reduction and analysis.

2.1. *Radio Observations*

At radio frequencies, the object was monitored using the University of Michigan Radio Astronomy Observatory (UMRAO) 26 m telescope, at 4.8, 8, and 14.5 GHz; the 14 m Metsähovi Radio Telescope of the Helsinki University of Technology, at 22 and 37 GHz; and the 576 m ring telescope (RATAN-600) of the Russian Academy of Sciences, at 2.3, 3.9, 7.7, 11, and 22 GHz.

At the UMRAO, the source was monitored in the course of the ongoing long-term blazar monitoring program. The data were analyzed following the standard procedure described in Aller et al. (1985). As mentioned above, the sampling at the lower frequencies (4.5 and 8 GHz) was rather poor (about once every 1−2 weeks) and some individual errors were rather large due to source confusion problems with 3C 66B. At 14.5 GHz, a slightly better sampling of ∼1−2 observations per week, at least until the end of 2003, was achieved with relative flux errors of typically a few percent. The resulting 14.5 GHz light curve is included in Figure 1. It seems to indicate generally moderate variability ($\Delta F/F \lesssim 25\%$) on timescales of ≳1 week, although a discrete autocorrelation analysis (Edelson & Krolik 1988) does
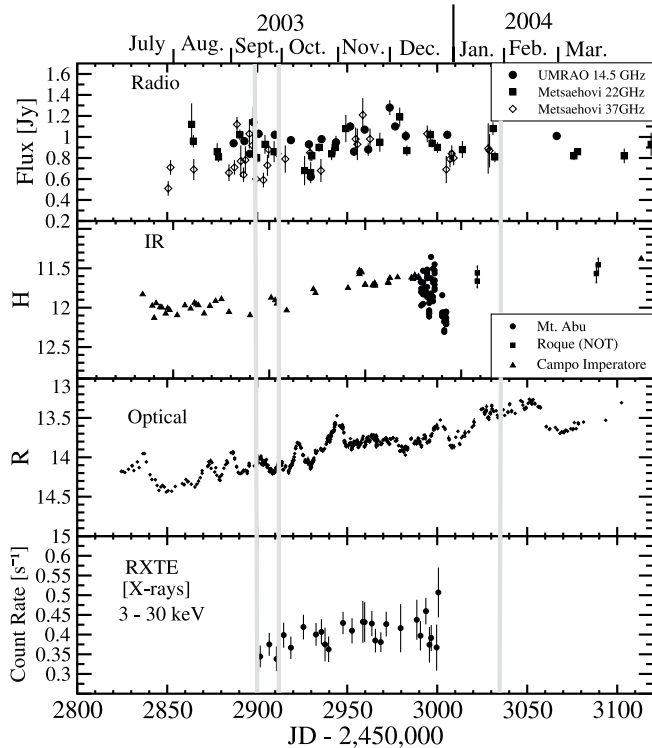
Fig. 1.—Time line of the broadband campaign on 3C 66A in 2003–2004. The gray vertical lines indicate the epochs of the VLBA observations.

not reveal any significant structure, primarily due to the insufficient sampling.

At 22 and 37 GHz, 3C 66A has been monitored using the 14 m radio telescope of the Metsähovi Radio Observatory of the Helsinki University of Technology. The data have been reduced with the standard procedure described in Teräsranta et al. (1998). The 22 and 37 GHz light curves reveal moderate-amplitude ($\Delta F/F \lesssim 30\%$), erratic variability that is clearly undersampled by the available data. The discrete autocorrelation functions indicate a timescale of a few days for this short-term variability.

We point out that the observed erratic variability may, at least in part, be a consequence of interstellar scintillation. At the Galactic coordinates of the source, the transition frequency, where the interstellar scattering strength (a measure of the phase change induced by interstellar scattering) becomes unity, is ~7 GHz (Walker 1998). At higher frequencies, as considered here, scattering will occur in the weak scattering regime, with only small phase changes through interstellar scattering. In this regime, we find fractional rms variability amplitudes for a point source due to interstellar scintillation of 0.36 and 0.09 at frequencies of 14.5 and 37 GHz, respectively, and the respective variability timescales due to interstellar scintillation are 1.4 and 0.9 hr. Consequently, in particular at lower frequencies ($\lesssim$20 GHz), a substantial fraction of the observed variability may well be due to interstellar scintillation.

The RATAN-600 has monitored 3C 66A, performing 17 observations from mid-1997 through 2003 October. The last two of these observations (October 11 and 14) coincided with our core campaign and provided additional frequency coverage at 2.3, 3.9, 7.7, 11, and 22 GHz. Those data were analyzed as described in detail in Kovalev et al. (1999), and the time average of the resulting fluxes from the two observations in 2003 October are included in the SED shown in Figure 15.

A total of nine observing epochs using the VLBA[44] have been approved to accompany our multiwavelength campaign on 3C 66A. In this paper we describe details of the data analysis and results of the first (2003.78; VLBA observing code BS133A), the second (2003.83; BS133B), and the fourth (2004.08; BS133E) epochs, concentrating on the results at 22 and 43 GHz. The third epoch (2003.96) suffered from radio frequency interference, and its reduction is in progress. Results of the complete set of all nine VLBA observing epochs, including all six frequencies (2.3, 5, 8.4, 22, 43, and 86 GHz) together with polarization data, will be presented in a separate paper (T. Savolainen et al. 2005, in preparation).

The data were correlated on the VLBA correlator and were postprocessed with the NRAO Astronomical Image Processing System, AIPS (Greisen 1988), and the Caltech DIFMAP package (Shepherd 1997). Standard methods for VLBI data reduction and imaging were used. A priori amplitude calibration was performed using measured system temperatures and gain curves in the AIPS task APCAL. At this point, a correction for atmospheric opacity was also applied. After removal of the parallactic angle phase, single-band delay and phase offsets were calculated manually by fringe-fitting a short scan of data of a bright calibrator source (0420−014). We did manual phase calibration instead of using pulse-cal tones, because there were unexpected jumps in the phases of the pulse-cal during the observations. Global fringe-fitting was performed with the AIPS task FRING using Los Alamos (LA) as a reference antenna. The AIPS procedure CRSFRING was used to remove the delay difference between right- and left-hand systems (this is needed for polarization calibration). A bandpass correction was determined and applied before averaging across the channels, after which the data were imported into DIFMAP.

In DIFMAP, the data were first phase self-calibrated using a point source model and then averaged in time. We performed data editing in a station-based manner and ran several iterations of CLEAN and phase self-calibration in Stokes I. After a reasonable fit to the closure phases was obtained, we also performed amplitude self-calibration, first with a solution interval corresponding to the whole observation length. The solution interval was then gradually shortened as the model improved by further CLEANing. Final images were produced using the Perl library FITSplot.[45] For final images, normal weighting of the uv-data was used in order to reveal the extended, low surface brightness emission.

We have checked the amplitude calibration by comparing the extrapolated zero baseline flux density of the compact source 0420−014 to the single-dish flux measurements at Metsähovi. The fluxes are comparable: at 22 GHz the VLBI flux is on average 5% lower than the single-dish flux, and the 43 GHz flux is on average 8% lower than the nearly simultaneous single-dish measurements at 37 GHz. The small amount of missing flux is probably due to some extended emission resolved out in the high-frequency VLBI images. The integrated VLBI flux of 3C 66A is about 30% smaller than the corresponding single-dish value at both 22 and 43 GHz, but since the source has notable kiloparsec-scale structure evident in the VLA images (Price et al. 1993; Taylor et al. 1996), it is most likely that the missing flux comes from this kiloparsec-scale jet, which is resolved out in our VLBI images. Thus, we conclude that the

TABLE 1
List of Observatories that Contributed Data to This Campaign

Observatory	Specifications	Frequency/Filters/Energy Range	N_{obs}
Radio Observatories			
UMRAO, Michigan, USA............................	26 m	4.8, 8, 14.5 GHz	46
Metsähovi, Finland	14 m	22, 37 GHz	103
RATAN-600, Russia	576 m (ring)	2.3, 3.9, 7.7, 11, 22 GHz	17
VLBA..	10×25 m	2.3, 5, 8.4, 22, 43, 86 GHz	9
Infrared Observatories			
Campo Imperatore, Italy................................	1.1 m	J, H, K	171
Mount Abu, India (MIRO)............................	1.2 m (NICMOS3)	J, H, K'	79
Roque (NOT), Canary Islands......................	2.56 m	J, H, K	15
Optical Observatories			
Abastumani, Georgia (FSU)	70 cm	R	210
Armenzano, Italy	40 cm	B, V, R, I	315
Bell Obs., Kentucky, USA	60 cm	R	12
Boltwood, Canada...	40 cm	B, V, R, I	402
Catania, Italy...	91 cm	U, B, V	835
Crimean Astron. Obs., Ukraine.....................	70 cm ST-7	B, V, R, I	85
Heidelberg, Germany.....................................	70 cm	B, R, I	8
Kitt Peak (MDM), Arizona, USA	130 cm	B, V, R, I	147
Michael Adrian Obs., Germany	120 cm	R	30
Mount Lemmon, South Korea.......................	100 cm	B, V, R, I	399
Mount Maidanak, Uzbekistan	150 cm AZT-22	B, R	1208
Nyrölä, Finland..	40 cm SCT	R	159
Osaka, Japan	51 cm	R	1167
Perugia, Italy...	40 cm	V, R, I	140
Roque (KVA), Canary Islands	35 cm	B, V, R	653
Roque (NOT), Canary Islands	256 cm	U, B, V, R, I	52
Sabadell, Spain	50 cm	B, R	4
San Pedro Martír, Mexico	150 cm	B, V, R, I	185
Shanghai, China...	156 cm	V, R	36
Skinakas, Crete	130 cm	B, V, R, I	156
Sobaeksan, South Korea................................	61 cm	B, V, R, I	133
St. Louis, Missouri, USA	35 cm	B, R	16
Torino, Italy	105 cm REOSC	B, V, R, I	227
Tuorla, Finland..	103 cm	B, V, R	1032
X-Ray Observatory			
RXTE	PCA	3–25 keV	26
γ-Ray Observatories			
STACEE...	Solar-Tower Cerenkov Array	>100 GeV	85
VERITAS..	Whipple 10 m	>390 GeV	31

accuracy of the amplitude calibration is better than 10% at both frequencies.

In order to estimate the parameters of the emission regions in the jet, we did model fitting to the self-calibrated visibilities in DIFMAP. The data were fitted with circular Gaussian model components, and we sought to obtain the best possible fit to the visibilities and to the closure phases. Several starting points were tried in order to avoid a local minimum fit. The results of this fitting procedure are included in Figures 2 and 3. In all the model fits, the core of the VLBI jet is the northernmost and also the brightest component. Beyond the core, we have divided the jet into three regions named A, B and C. Closest to the core is region C, which consists of three components with decreasing surface brightness as a function of the distance from the core. Region B, also made of three components, shows a clear bending of the jet together with rebrightening. The observed increase

in the flux at this point could plausibly be due to increased Doppler boosting caused by the bending of the jet toward our line of sight. Region A shows weak extended emission at 8 mas from the core at 22 GHz. This emission is more pronounced at lower frequencies.

Figure 4 shows the separation of the model components from the core, at each epoch. Components A–C are weak compared to the core (see Table 2), which renders the estimation of errors of the model parameters using programs like Difwrap (Lovell 2000) problematic. Thus, in Figure 4 we have assumed the following uncertainties in the component position accuracy: (1) for bright features with signal-to noise ratio >50, the positions are accurate to 20% of the projection of the elliptical beam FWHM onto a line joining the center of the core to the center of the components; (2) for weaker components with signal-to-noise ratio <50, uncertainties are 50% of the beam size or 50% of the
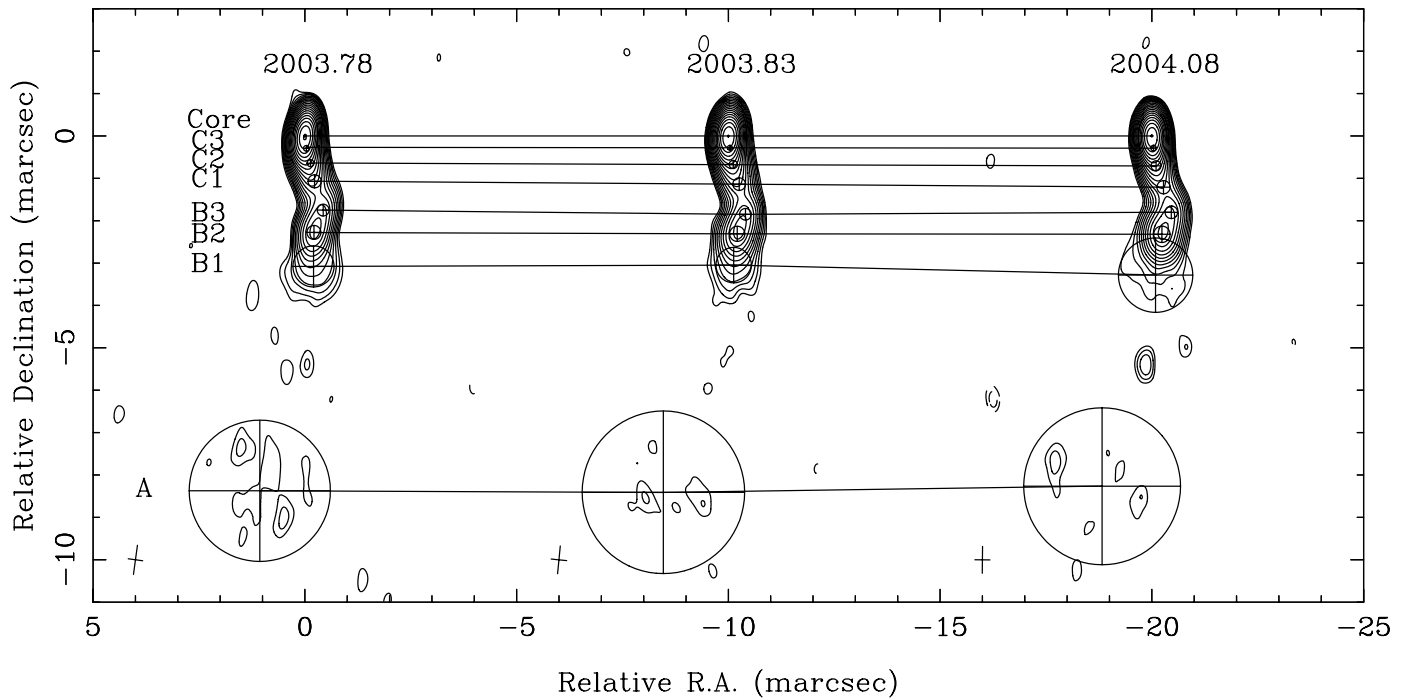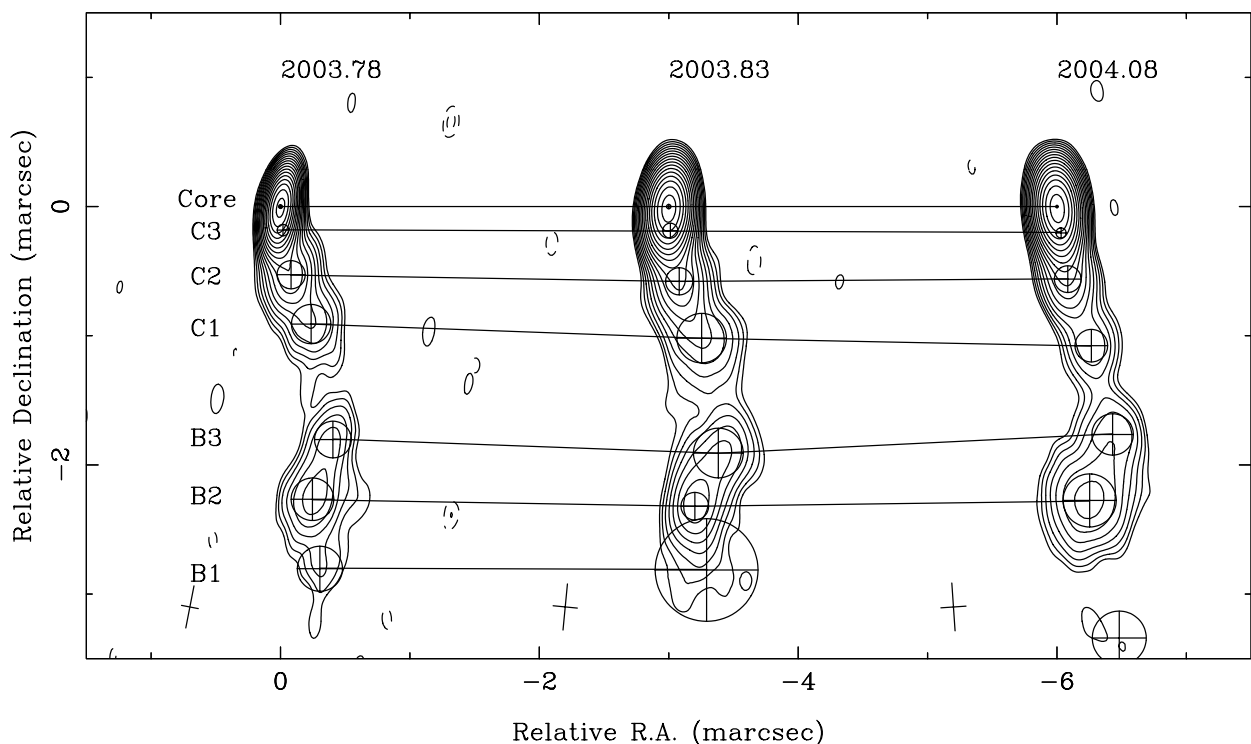
Fig. 2.—22 GHz VLBA maps of 3C 66A during the three epochs in 2003–2004 contemporaneous with our campaign. Overlaid are the fit results from decomposing the structure into a sum of Gaussian components.

size of the knot—whichever is larger. These estimates are based on the experience with other sources (T. Savolainen et al. 2005, in preparation; K. Wiik et al. 2005, in preparation), and they follow the results by Jorstad et al. (2005), where uncertainties of model fit parameters for a large number of observations are estimated. Positional errors of similar size are also reported by Homan et al. (2001), who have estimated the uncertainties

from the variance of the component position about the best-fit polynomial.

There is a ∼0.1 mas shift of the components C1–C3 between the two frequencies, with the 22 GHz model components appearing further downstream. This cannot be explained by an opacity effect, since in that case the components would have shifted in the opposite direction: at higher frequency we would

Fig. 3.—43 GHz VLBA maps of 3C 66A during the three epochs in 2003–2004 contemporaneous with our campaign. Overlaid are the fit results from decomposing the structure into a sum of Gaussian components.
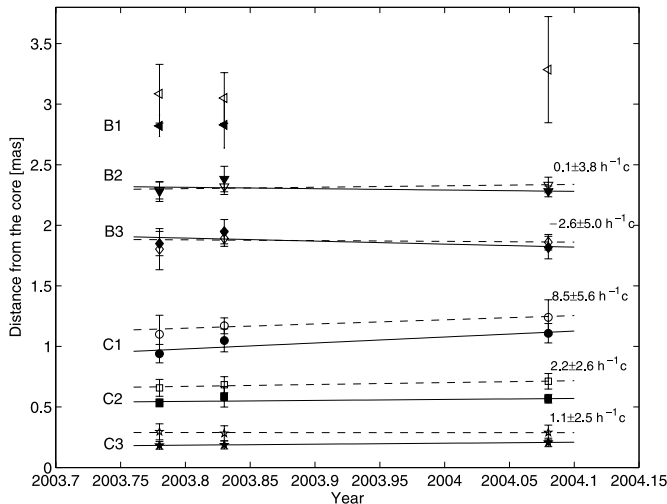
Fig. 4.—Separation from the core of the Gaussian fit components shown in Figs. 2 and 3, as a function of time. Filled symbols refer to 22 GHz, open symbols to 43 GHz. The solid (dashed) lines show linear least-squares fits to the positions of 22 (43) GHz components. The velocity results are the average of the results from the two frequencies. All components except C1 are consistent with being stationary.

expect to see emission from the region closer to the apex of the jet than at lower frequency, if the opacity effect is significant. This obviously is not the case in Figure 4, and moreover, for the components B2 and B3 the positions at 22 and 43 GHz are coincident. However, there is a simple explanation for the observed shift, if the brightness profile along the jet in region C is smooth. Namely, the flux in the outer part of region C decreases more steeply at 43 GHz than at 22 GHz (see Figs. 2 and 3). As region C is modeled by the same number of components at both frequencies, the model-fit procedure shifts the 22 GHz components downstream relative to 43 GHz components in order to represent the power law.

Figure 4 shows that, except for one component, all the components revealed by the analysis of the three epochs considered here are consistent with zero proper motion. Although a monitoring effort over a longer timescale will be necessary to settle this issue, our analysis shows slower component motion than what is presented by Jorstad et al. (2001), where fast superluminal motions of several components with speeds ranging from 9 to 19 h^{-1} c were found. Note, however, that the data used by Jorstad et al. (2001) covered a much longer time frame and refers to different components and a rather different state of activity of 3C 66A. Moreover, there are also similarities between the data sets: Jorstad et al. (2001) reported a stationary component (their component "C") at a distance of ∼0.5 mas from the core, which could correspond to our component C2. New 7 mm VLBA monitoring data presented in a recent paper by Jorstad et al. (2005) suggest that there are two kinds of components in 3C 66A: fast and very weak components with apparent speeds >20 c, and stronger components with moderate velocities of 1.5−5 c. The components C1−C3 in our analysis could be qualitatively similar to the latter. More solid conclusions concerning the question of superluminal motions of individual components might be possible after the final analysis of all nine epochs of the entire VLBA monitoring program of 3C 66A proposed in connection with this campaign (T. Savolainen et al. 2005, in preparation). Based on the analysis of the three epochs contemporaneous with the other observations of this campaign, one component, C1, shows superluminal motion of (8.5 ± 5.6) h^{-1} $c = (12.1 \pm 8.0)$ c for $h = 0.7$.

The essentially zero proper motion of most of the components together with the observed trend of the brightness temperature versus distance along the jet (see § 6.2) suggests that in the case of 3C 66A the VLBA model-fit components might not correspond to actual "knots" in the jet, but a rather smooth flow with simple brightness profile (such as a power law) might better describe the jet during this campaign—at least in region C. More detailed parameter estimates will be extracted from these results in § 6.2.

2.2. Infrared Observations

In the context of the extensive WEBT campaign (see § 2.3), 3C 66A was also observed at near-IR wavelengths in the J, H, and K/K' bands at three observatories: the Campo Imperatore 1.1 m telescope of the Infrared Observatory of the Astronomical Observatory of Rome, Italy; the 1.2 m telescope (using the NICMOS3 HgCdTe IR array with 256 × 256 pixels, with each pixel corresponding to 0″.96 on the sky) at the Mount Abu Infrared Observatory (MIRO) at Mount Abu, India; and the 2.56 m Nordic Optical Telescope (NOT) on Roque de los Muchachos on the Canary Island of La Palma. The primary data were analyzed using the same standard technique as the optical data (see § 2.3), including flat-field subtraction, extraction of instrumental magnitudes, calibration against comparison stars to obtain standard magnitudes, and dereddening. The sampling was generally not dense enough to allow an improvement of the data quality by rebinning. Unfortunately, the three observatories did not perform any observations on the same day, so that the cross-calibration between different instruments is problematic. We have therefore opted not to correct for possible systematic offsets beyond the calibration to standard magnitudes of well-calibrated comparison stars (see § 2.3).

The resulting H-band light curve is included in Figure 1, and a comparison of all three IR-band light curves (J, H, and K/K') is shown in Figure 5. Generally, we find moderate variability of $\Delta(J, H, K/K') \lesssim 0.2$ within ∼ a few days. The various infrared bands trace each other very well, and there does not appear to be any significant time lags between the different bands. It is obvious that there are issues with the cross calibration between the three observatories. In particular, the Mount Abu observations (using the J, H, and K' filters) in mid-December of 2003 indicate a significant drop of the average level of near-IR flux. While there appears to be a similar flux drop around the same time in the radio light curves, the much more densely sampled optical light curves do not indicate a similar feature. However, it is obvious that the near-IR data around this time exhibit an unusually large scatter (by ∼0.5 mag on subhour timescales), they may be affected by calibration uncertainties. We note that rebinning of the IR data in time bins of up to 30 minutes did not improve the quality of the data because of the extreme nature of the apparent flux fluctuations. We also point out that the use of the K' filter at Mount Abu versus the K filter at the other two IR observatories could only explain offsets of less than the individual measurement errors, so this effect was neglected in our analysis.

2.3. Optical Observations

In the optical component of the extensive WEBT campaign, 24 observatories in 15 countries contributed 7611 individual photometric data points. The observing strategy and data analysis followed to a large extent the standard procedure described previously for a similar campaign on BL Lac in 2000 (Villata et al. 2002). For more information about WEBT campaigns, see

TABLE 2
VLBA Component Fluxes, Core Distances, Position Angles,
and Circular Diameters

Frequency (GHz)	Component ID	Flux (mJy)	Core Distance (mas)	Position Angle (deg)	Diameter (mas)
		Epoch 2003.78			
22...............................	Core	387	0.0	0.0	0.047
	C3	61	0.295	−172.9	0.136
	C2	36	0.658	−168.2	0.164
	C1	19	1.096	−167.9	0.309
	B3	21	1.803	−166.1	0.278
	B2	40	2.287	−174.6	0.331
	B1	19	3.086	−176.2	0.970
	A	37	8.439	172.8	3.333
43...............................	Core	355	0.0	0.0	0.029
	C3	63	0.183	−174.0	0.089
	C2	43	0.534	−171.1	0.218
	C1	24	0.940	−165.4	0.304
	B3	18	1.849	−167.3	0.284
	B2	30	2.279	−173.8	0.329
	B1	9	2.821	−173.8	0.349
		Epoch 2003.83			
22...............................	Core	375	0.0	0.0	0.032
	C3	59	0.282	−172.4	0.118
	C2	38	0.685	−170.2	0.193
	C1	18	1.167	−167.3	0.298
	B3	23	1.892	−167.7	0.274
	B2	39	2.320	−174.8	0.358
	B1	13	3.051	−177.6	0.836
	A	41	8.546	169.7	3.836
43...............................	Core	369	0.0	0.0	0.034
	C3	76	0.187	−176.3	0.116
	C2	34	0.584	−172.1	0.210
	C1	26	1.050	−166.0	0.383
	B3	26	1.947	−168.6	0.385
	B2	20	2.328	−175.0	0.213
	B1	16	2.829	−174.1	0.795
		Epoch 2004.08			
22...............................	Core	363	0.0	0.0	0.046
	C3	64	0.289	−172.4	0.132
	C2	32	0.712	−172.0	0.235
	C1	12	1.241	−167.2	0.311
	B3	22	1.860	−165.7	0.296
	B2	45	2.333	−174.2	0.386
	B1	18	3.285	−178.5	1.754
	A	38	8.348	171.9	3.702
43...............................	Core	372	0.0	0.0	0.019
	C3	59	0.207	−171.2	0.078
	C2	30	0.568	−171.6	0.207
	C1	13	1.109	−166.2	0.252
	B3	15	1.816	−166.3	0.320
	B2	40	2.289	−173.7	0.411
	X1	4	3.375	−171.8	0.417

also Villata et al. (2000, 2002, 2004a, 2004b) and Raiteri et al. (2001, 2005).

It had been suggested that, optimally, observers perform photometric observations alternately in the B and R bands, and include complete $(U)BVRI$ sequences at the beginning and the end of each observing run. Exposure times should be chosen to obtain an optimal compromise between high-precision (instrumental errors less than $\sim$0.03 mag for small telescopes and

$\sim$0.01 mag for larger ones) and high time resolution. If this precision requirement leads to gaps of 15–20 minutes in each light curve, we suggested carrying out observations in the R band only. Observers were asked to perform bias (dark) corrections, as well as flat-fielding on their frames, and obtain instrumental magnitudes, applying either aperture photometry (using IRAF or CCDPHOT) or Gaussian fitting for the source 3C 66A and the comparison stars 13, 14, 21, and 23 in the tables of González-Pérez et al.
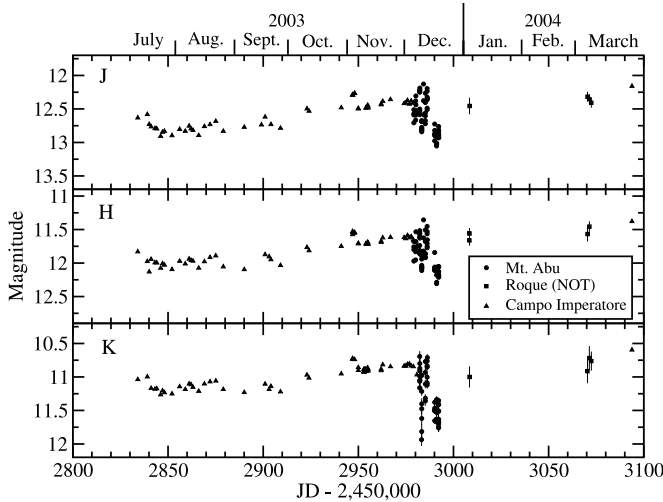
Fig. 5.—Light curves in the near-IR *J*, *H*, and *K* bands over the entire duration of the campaign.

(2001), where high-precision standard magnitudes for these stars have been published. This calibration has then been used to convert instrumental to standard photometric magnitudes for each data set. In the next step, unreliable data points (with large error bars at times when higher quality data points were available) were discarded. Our data did not provide evidence for significant variability on subhour timescales. Consequently, error bars on individual data sets could be further reduced by rebinning on timescales of typically 15–20 minutes.

Finally, there may be systematic offsets between different instruments and telescopes. Wherever our data sets contained sufficient independent measurements to clearly identify such offsets, individual data sets were corrected by applying appropriate correction factors. In the case of BL Lac and similar sources (e.g., Villata et al. 2002), such corrections need to be done on a night-by-night basis since changes in the seeing conditions affect the point-spread function and thus the precise amount of the host galaxy contamination. However, in the absence of a significant host galaxy contribution, these systematic effects should be purely instrumental in nature and should thus not depend on daily seeing conditions. Thus, we opted to introduce only global correction factors for entire single-instrument data sets on 3C 66A. This provided satisfactory results without obvious residual inter-instrumental inconsistencies. The resulting offsets are listed in Table 3.

In order to provide information on the intrinsic broadband spectral shape (and, in particular, a reliable extraction of $B - R$ color indices), the data were dereddened using the Galactic extinction coefficients of Schlegel et al. (1998), based on $A_B = 0.363$ mag and $E(B - V) = 0.084$ mag.[46] As mentioned in the introduction, the R magnitude of the host galaxy of 3C 66A is ~19 mag, so its contribution is negligible, and no host-galaxy correction was applied.

2.3.1. *Light Curves*

As a consequence of the observing strategy described above, the R- and B-band light curves are the most densely sampled ones, resulting in several well-sampled light curve segments over $\sim5-10$ days each, with no major interruptions, except for a

[46] See http://nedwww.ipac.caltech.edu.

TABLE 3
INTERINSTRUMENTAL CORRECTION OFFSETS FOR OPTICAL DATA

Observatory	B	V	R	I
Armenzano, Italy	+0.02	...	+0.02	...
Bell Obs., Kentucky, USA	...	...	...	...
Boltwood, Canada	−0.02	...	...	...
Catania, Italy	...	...	...	...
Crimea, Astron. Obs., Ukraine	...	+0.03	...	...
Heidelberg, Germany	...	...	...	...
Kitt Peak (MDM), Arizona, USA	...	...	...	...
Michael Adrian Obs., Germany	...	...	...	...
Mount Lemmon, South Korea	...	...	...	...
Mount Maidanak, Uzbekistan	+0.01	...	...	...
Nyrola, Finland	...	...	−0.03	...
Osaka, Japan	...	...	...	...
Perugia, Italy	...	+0.08	+0.05	+0.04
Roque (NOT), Canary Islands	...	...	...	...
Sabadell, Spain	...	...	...	...
San Pedro Martír, Mexico	+0.08	...	+0.07	...
Shanghai, China	...	...	−0.03	...
Skinakas, Crete	−0.01	−0.04	−0.04	−0.05
Sobaeksan, South Korea	...	...	...	...
St. Louis, Missouri, USA	−0.06	...	...	...
Torino, Italy	−0.09	...	...	−0.03
Tuorla, FInland	...	+0.02	−0.02	−

gap of a few hours due to the lack of coverage when 3C 66A would have been optimally observable from locations in the Pacific Ocean. The R-band light curve over the entire duration of the campaign is included in Figure 1 and compared to the light curves at all other optical bands in Figure 6. These figures illustrate that the object underwent a gradual brightening throughout the period 2003 July to 2004 February, reaching a maximum at $R \approx 13.4$ on 2004 February 18, followed by a sharp decline by $\Delta R \sim 0.4$ mag within ~15 days. On top of this overall brightening trend, several major outbursts by $\Delta R \sim 0.3-0.5$ mag on timescales of ~10 days occurred. The two most dramatic ones of these outbursts peaked on 2003 July 18 and November 1. Details of the November 1 outburst are displayed in Figures 7–9. We find evidence for intraday microvariability of $\Delta R \sim 0.05$ mag on timescales down to ~2 hr. One example for such evidence is illustrated in Figure 10,
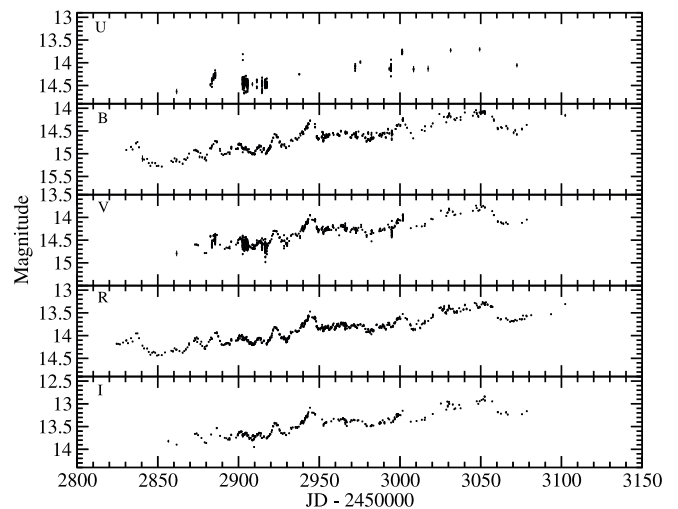

Fig. 6.—Light curves in the optical *UBVRI* bands over the entire duration of the campaign.
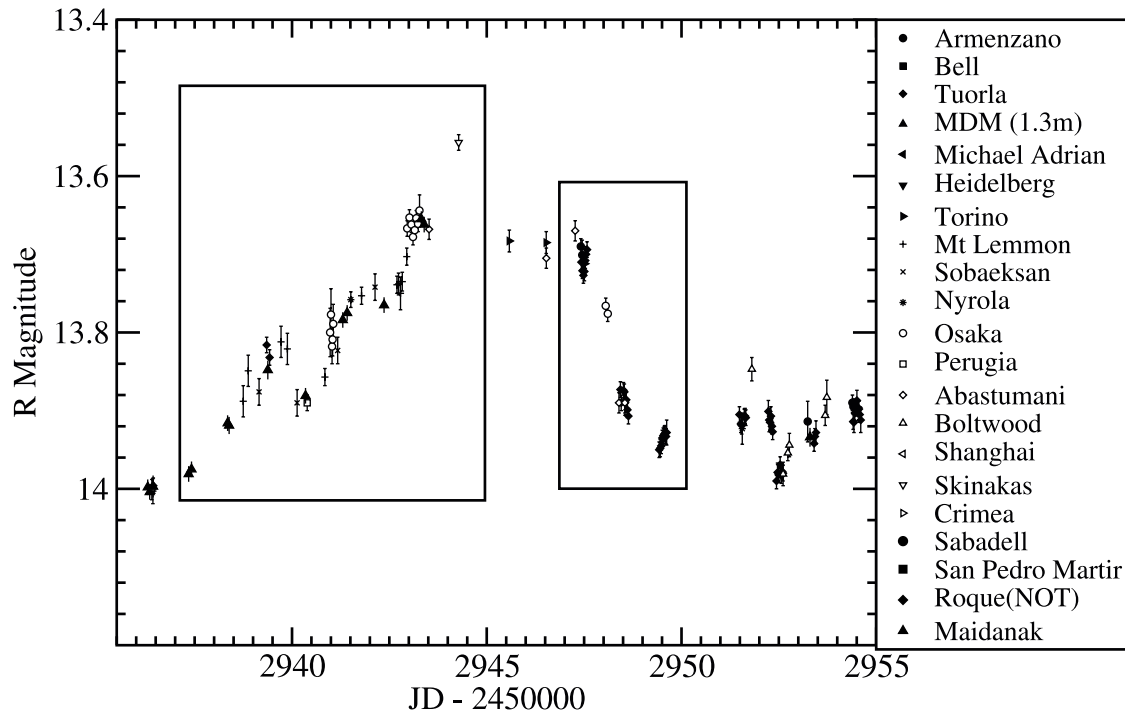
FIG. 7.—Details of the *R*-band light curve during the major outburst around 2003 November 1. The boxes indicate the light curve segments shown in more detail in Figs. 8 and 9.

which shows the intranight data from the Torino Observatory for JD 2,452,955 (=2003 November 11). The figure presents the instrumental magnitudes of 3C 66A, comparison star A, and the difference of both. While the difference seems to be affected by seeing effects at the beginning and end of the observation (rising and falling in tandem with the instrumental magnitudes), there is evidence for intraday variability around ∼JD 2,452,955.5, where there were only very minor changes in the atmospheric opacity.

Visual inspection of individual major outbursts suggests periods of more rapid decline than rise.

2.3.2. *Periodicity Analysis*

For several blazars, including 3C 66A, periodicities on various timescales, from several tens of days to several years, have been claimed (see, e.g., Rieger 2004 and references therein for a more complete discussion). In order to search for a possible periodicity in the optical *R*-band light curve from our WEBT
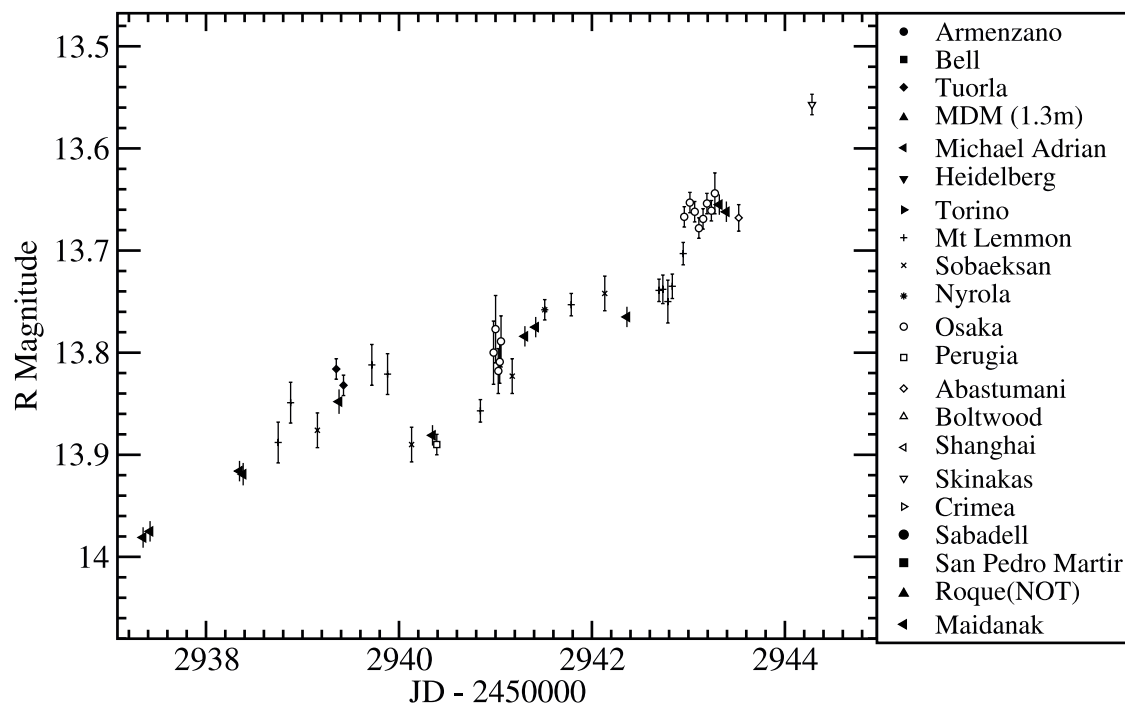
FIG. 8.—Details of the *R*-band light curve during the rising phase of the major outburst around 2003 November 1.
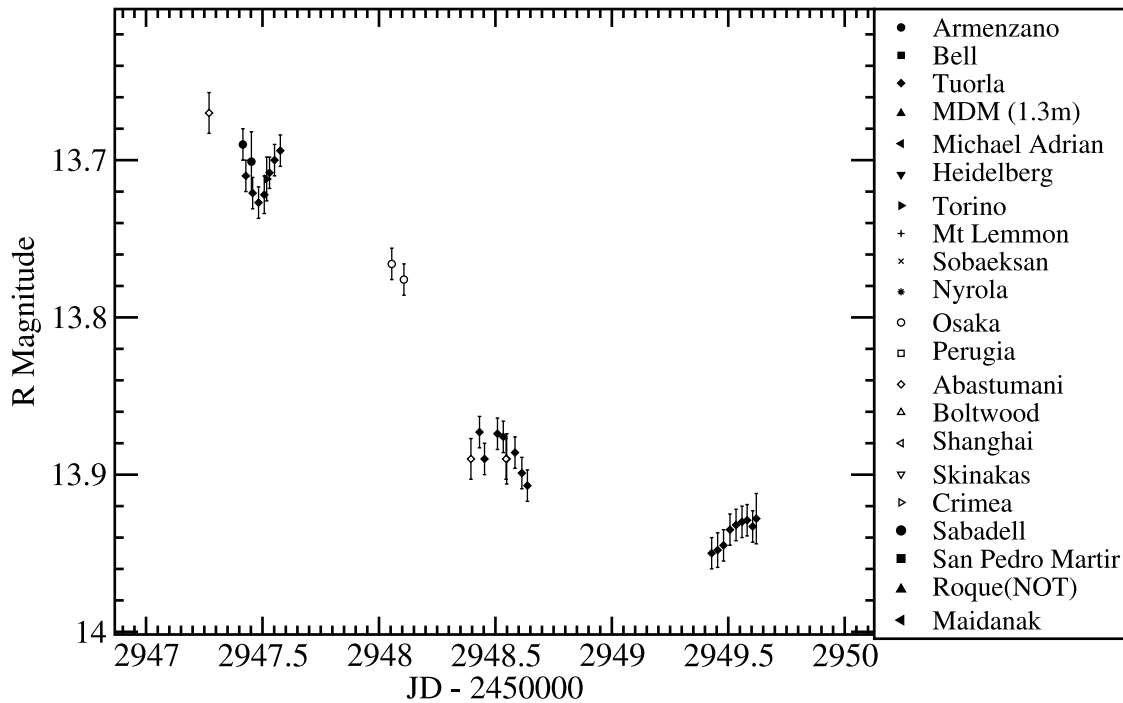
FIG. 9.—Details of the *R*-band light curve during the decaying phase of the major outburst around 2003 November 1.

campaign, we have performed a Fourier analysis of the *R*-band light curve after interpolation of the light curve over the (short) gaps in the available data. Such an analysis becomes unreliable for periods of more than ∼1/10 of the length of the data segment. Consequently, our data can be used for a meaningful analysis on timescales of $\tau \lesssim 30$–50 days. No evidence for a periodicity in this range has been found. However, we note a sequence of large outbursts on 2003 July 18 (MJD 52,838), September 5 (MJD 52,887), November 1 (MJD 52,944), and December 28 (MJD 53,001), and 2004 February 18 (MJD 53,053), which are separated by intervals of 49, 57, 57, and 52 days, respectively. These intervals appear remarkably regular, and only slightly shorter than the 65 day period claimed by Lainela et al. (1999). The duration of

our monitoring campaign is too short to do a meaningful analysis of the statistical significance of this quasi-periodicity. This question will be revisited in future work, on the basis of a larger data sample, including archival optical data.

2.4. *X-Ray Observations*

3C 66A was observed by the *Rossi X-Ray Timing Explorer* (*RXTE*) 26 times between 2003 September 19 and December 27, for a total observation time of approximately 200 ks. Analysis of the *RXTE* PCA data was carried out using faint-source procedures as described in the *RXTE* Cookbook. Standard selection criteria were used to remove disruptions from the South Atlantic Anomaly, bright Earth, instrument mispointing, and electron contamination. For the entire data set, only PCUs 0 and 2 were activated, but data from PCU 0 were discarded due to its missing propane veto. There is also a persistent problem in the background model of the PCA around the 4.78 keV xenon L edge, which causes a small anomaly in count rates near this energy. For faint sources like 3C 66A, this anomaly can be significant, so photons in the three energy bins surrounding this energy were discarded.

Photons from 3–10 keV were extracted from the data using only the top layer of PCU2. Extracting higher energy photons proved unreliable, as the source flux was close to the PCA source-confusion limit. A spectrum was compiled using data from all 26 source observations. The spectrum was fit to a simple power law, which resulted in an energy spectral index of $\alpha = 1.47 \pm 0.56$ and a flux $\Phi_{1\,\mathrm{keV}} = (4.06 \pm 0.49) \times 10^{-3}$ photons cm^{-2} s^{-1} keV^{-1}, with $\chi^2/n = 13.6/14$. Galactic absorption was not included in the fit model, as the lack of data below 3 keV precludes a useful constraint on N_{H}. A plot of the spectrum and fit is shown in Figure 11.

The PCA is a nonimaging instrument with a FWHM response of $1°$, so there is the potential that the signal found here is a sum over multiple sources. Most notably, the FR-1 galaxy 3C 66B lies only 6′ from 3C 66A and is a known X-ray emitter. Although indistinguishable from 3C 66A with the PCA, its typical flux is
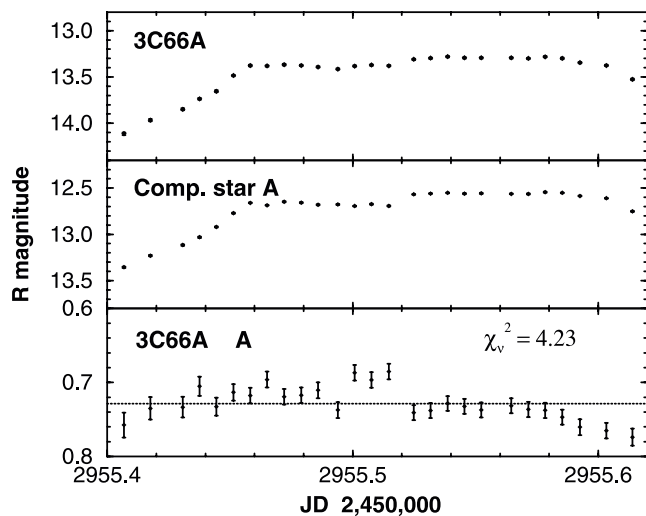

FIG. 10.—Instrumental magnitudes of 3C 66A (*top panel*) and comparison star A (*middle panel*) of the University of Torino data of JD 2,452,955 (=2003 November 11) The difference (*bottom panel*) shows clear evidence for intra-night variability during the central portion of this observation (∼JD 2,452,955.4 to 2,452,955.5).
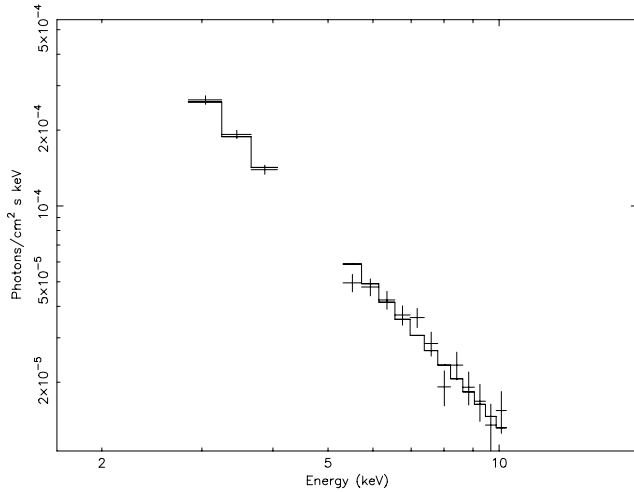
Fig. 11.—Average *RXTE* spectrum (3–10 keV) and power-law fit for all observations of 3C 66A taken as part of the multiwavelength campaign. See text for best-fit parameters.

at a level of ~2% of the measured PCA flux of 3C 66A (Croston et al. 2003), and it is thus not a significant contributor. In the 3EG catalog, there is also confusion of 3C 66A with a nearby pulsar, PSR J0218+4232. At a source separation of 58′, the PCA response for the pulsar is low for 3C 66A pointed observations, and thus it does not make a significant contribution.

The 3–10 keV photons were binned into 24 hr periods to render a light curve, which is included in Figure 1. No significant flux variations or transient events were seen. To check for spectral variations, the data set was divided into four roughly equal subperiods and power-law spectra were fitted to each subperiod. Fits to all four subperiods were consistent with the spectral parameters obtained from the entire data set, and all subperiods were consistent with each other. From this we conclude that there were no variations of either flux or spectral shape in the X-ray band during the observing period within the detection capabilities of *RXTE*.

2.5. *Gamma-Ray Observations*

At VHE γ-rays, 3C 66A was observed contemporaneously with our broadband campaign by STACEE and by the 10 m Whipple Telescope of the VERITAS collaboration.

STACEE took a total of 85 28 minute on-off pairs of data, totaling 33.7 hr of live time on-source. After data-quality cuts and padding, a total of 16.3 hr of on-source live time remained. A net on-source excess of 1134 events attributed to photons of energy $E > 100$ GeV was seen against a background of 231,742 events. The details of the STACEE data analysis are published in a separate paper (Bramel et al. 2005).

TABLE 4
VHE Photon Flux 99.9% Confidence Upper Limits from the STACEE Observations for Various Assumptions of an Underlying Intrinsic Photon Spectral Index $\Gamma = \alpha + 1$

Γ	E_{thr} (GeV)	dN/dE at E_{thr} (photons m^{-2} s^{-1} GeV^{-1})
2.0	200	5.23×10^{-9}
2.5	184	9.39×10^{-9}
3.0	150	2.26×10^{-8}
3.5	147	3.10×10^{-8}

TABLE 5
Observation Log and 99% Confidence Upper Limits on the Integrated >390 GeV Photon Flux from the Whipple Observations of 3C 66A, Assuming a Crab-like Spectrum

Date	Start Time (UTC)	On-Source Live Time (minutes)	99.9% Upper Limit (10^{-11} ergs cm^{-2} s^{-1})
2003 Sep 27	10:57	27.73	2.05
2003 Sep 28	09:04	27.70	3.16
2003 Sep 29	08:16	27.75	2.73
2003 Oct 2	08:58	27.66	1.77
	09:27	27.73	2.35
	10:25	27.69	1.82
2003 Oct 23	06:58	27.55	6.19
2003 Oct 24	07:07	27.57	5.65
2003 Oct 28	06:40	27.55	6.35
2003 Oct 28	07:08	27.57	7.00
2003 Oct 29	06:41	27.57	6.62
	08:15	19.99	5.29
2003 Oct 30	06:27	27.61	4.39
2003 Nov 1	07:17	27.58	4.51
2003 Nov 25	05:49	27.55	6.32
2003 Nov 28	04:42	27.57	2.81
2003 Dec 14	03:06	27.62	4.87
2003 Dec 17	03:00	27.63	5.95
	04:08	27.54	5.23
	04:37	27.58	5.23
	05:05	27.55	6.71
	05:33	27.58	3.67
2003 Dec 20	03:38	27.63	2.60
	05:09	27.60	5.95
	06:07	27.66	4.45
2003 Dec 23	02:48	27.70	4.63
	04:01	27.71	4.03
	04:31	27.68	3.88
	04:59	27.70	2.94
2003 Dec 25	04:35	27.64	5.44
2004 Jan 13	02:17	27.58	5.23

The source excess quoted above corresponds to a significance of 2.2 σ, which is insufficient to claim a detection, but can be used to establish firm upper flux limits. For various assumptions of an underlying intrinsic source power-law spectrum, those upper limits are listed in Table 4. The data were also binned in 24 hr segments. This revealed no significant excess on any given day and thus no evidence for a statistically significant transient event during the campaign period.

The VERITAS collaboration observed 3C 66A during the period 2003 September 27 to 2004 January 13, obtaining a total of 31 on-off pairs with typically ~27.6 minutes of on-source live time per pair. The data were analyzed following the standard Whipple data analysis procedure (see, e.g., Falcone et al. 2004). The log of the individual observations and 99.9% confidence upper limits, assuming an underlying Crab-like source spectrum with an underlying energy index of 2.49 (Hillas et al. 1998), are listed in Table 5. Combining all measurements results in a 99.9% confidence upper limit of 0.91×10^{-11} ergs cm^{-2} s^{-1}.

3. SPECTRAL VARIABILITY

In this section we will describe spectral variability phenomena, i.e., the variability of spectral (and color) indices and their correlations with monochromatic source fluxes. As already mentioned in the previous section, no evidence for spectral variability in the X-ray regime was found. Consequently, we will concentrate here on the optical spectral variability as indicated by a change of
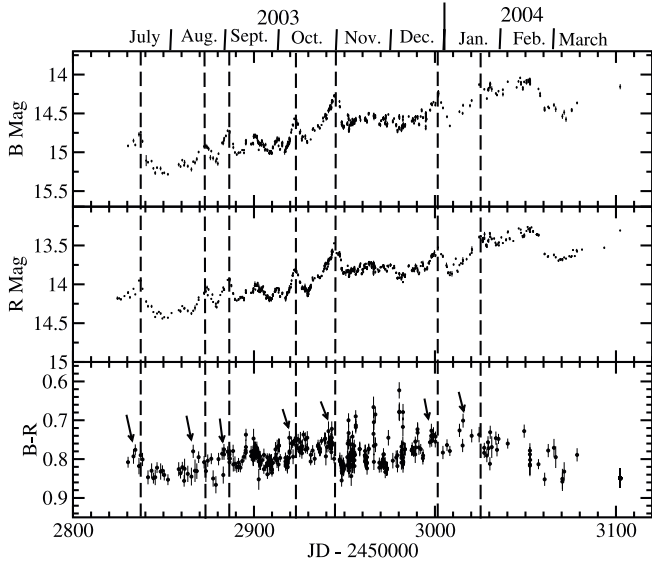
Fig. 12.—Light curve of the B and R magnitudes and the $B - R$ color index of 3C 66A over the duration of the entire campaign. While the B and R light curves are very well correlated, with no significant detection of a time delay, maxima of the spectral hardness (minima of $B - R$) systematically precede B and R outbursts by a few days.
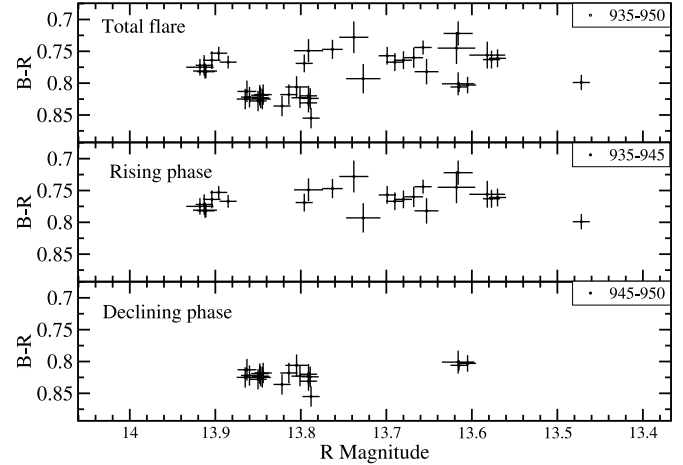

Fig. 14.—Optical hardness-intensity diagram for the flare around 2003 November 1. The optical spectrum already begins to soften significantly while the R-band flux is still rising at $R \lesssim 13.6$.

the optical color. In particular, our observing strategy was optimized to obtain a good sampling of the $B - R$ color index as a function of time.

Based on our observation (see § 2.3) of no significant variability on timescale less than ∼1 hr, we extracted $B - R$ color indices on measurements of B and R magnitudes separated by less than 20 minutes of each other. Figure 12 shows a comparison of the light curves of the B and R magnitudes and the $B - R$ color index. The figure reveals an interesting new result: while the B and R light curves are well correlated, with no significant detection of a time lag from a discrete correlation function (DCF) analysis (see § 4), maxima of the spectral hardness (i.e., minima of the value of $B - R$) seem to precede B- and R-band flux outbursts systematically by a few days. In other words, the optical spectra harden at the onset of a major outburst and continue to soften as the flare progresses through both the rising and the decaying phase. However, Figure 12 also indi-

cates that the apparent lead time of the $B - R$ hardness maximum varies within a range of a few days. This might be the reason that a cross-correlation analysis between the $B - R$ index and the B or R light curves does not reveal a strong peak. In fact, the DCF between those time series never exceeds values of ∼0.3 at all.

Also very interesting and intriguing is the $B - R$ behavior of the source from around JD 2,452,955 to 2,452,995, where no major flux outbursts are observed, but several episodes of significant spectral hardening by $\Delta(B - R) \gtrsim 0.1$ (corresponding to spectral-index variations of $\Delta\alpha_{\mathrm{opt}} \gtrsim 0.2$) are observed.

In Figure 13 we have plotted the $B - R$ index versus R-band magnitude for the entire data set. The plot shows that there is a weak indication of a positive hardness-intensity correlation at low-flux states with $R \gtrsim 14.0$. At higher flux levels, no correlation is apparent, which might be a consequence of the result found above, that the $B - R$ hardness actually peaks during the rising phase of individual outbursts. This is in contrast with recent results of Vagnetti et al. (2003), who, on the basis of a smaller data set, have found a consistent trend of $B - R$ hardening with increasing B-band flux, independent of the actual flux value.

The optical spectral hysteresis visible in our data is further illustrated in Figure 14, where we have plotted the $B - R$ versus R hardness-intensity diagram for the example of one individual outburst on 2003 November 1 (MJD 52,944). The top panel shows the hardness-intensity diagram for the entire flare, which is then split up into the rising and the decaying phases of the flare in the middle and lower panels, respectively. The figure illustrates that as the flare rises up to the peak R brightness, the spectrum already begins to soften significantly as $R \lesssim 13.6$. Similar trends are found for other optical flares as well. Possible physical interpretations of this trend, along with detailed modeling of the SED and spectral variability will be presented in a separate paper (M. Joshi & M. Böttcher 2005, in preparation).

4. INTERBAND CROSS CORRELATIONS AND TIME LAGS

In this section we investigate cross-correlations between the measured light curves at different frequencies, within individual frequency bands as well as broadband correlations between different frequency bands. Because of relatively poor sampling of the radio and IR light curves, our searches for correlations

Fig. 13.—Optical hardness-intensity diagram for the complete data set over the entire duration of the campaign. While a positive hardness-intensity correlation seems to be present at low brightness, $R \gtrsim 14.0$, no clear correlation can be found in brighter states.

between different radio and IR bands and between those wavelength bands with the optical ones on short timescales compared to the duration of our campaign did not return conclusive results. Also, in agreement with our nondetection of a periodicity on timescales of ≲50 days, a discrete autocorrelation function (Edelson & Krolik 1988) analysis of individual optical light curves did not return results beyond artificial "periodicities." Such artifacts can be attributed to the quasi-periodic, uneven time coverage, which results in spurious detections of periodicities at multiples of days and multiples of ∼0.5 days (the time delay between the peak coverage from the heavily contributing observatories in Europe and in East Asia). A discrete autocorrelation function analysis of the *R*-band light curve also revealed secondary peaks at ±4 days with a correlation coefficient close to 1.

The cleanest results of a DCF analysis are obviously expected for the most densely sampled light curves, which we obtained in the *B* and *R* bands. We performed DCFs between the *R*- and *B*-band light curves on a variety of timescales with a variety of binning intervals, ranging from 15 minutes to 10 days. On intraday timescales, we find consistently a sharp peak at 0 delay with all bin sizes we used, which indicates no evidence for a time delay between variability patterns in the *R* and *B* band reaching their peak fluxes in each band. The DCFs on short timescales are dominated by the artificial 0.5 and 1 day periodicities mentioned above. The DCF between *R*- and *B*-band magnitudes on timescales of several days seems to indicate a strong correlation at $\tau \sim -4$ days, corresponding to a lead of the *B* versus the *R* band. However, this might be a consequence of the probably artificial 4 day "periodicity" of the *R*-band light curve discussed in the previous paragraph, which prevents us from making any claim about the detection of a 4 day delay between the *R*- and *B*-band light curves on the basis of our DCF analysis.

5. BROADBAND SPECTRAL ENERGY DISTRIBUTIONS

From the various flux measurements described in detail in the previous sections, we can now compose contemporaneous SEDs of 3C 66A at various times during our campaign. Significant variability was only detected in the radio, IR, and optical bands. In those bands, we extracted SEDs for four epochs: during two major outbursts around 2003 November 1 and December 28, during a minor outburst around 2003 October 1, and during a rather quiescent state around 2003 November 11. Dereddened optical and near-IR magnitudes were converted to fluxes using the zero-point normalizations of Bessel et al. (1998). The resulting SEDs are plotted in Figure 15. Due to the relatively poor sampling, radio and IR data were often not quite simultaneous with the optical spectra, which were extracted near the peaks of the individual outbursts mentioned above. In this case, the closest near-IR and radio data points were chosen. This led to time offsets between the optical and the radio data points of up to ∼5 days. Given the relatively long timescale and moderate amplitude of variability at radio wavelengths, we are confident that this did not introduce serious distortions of the low-frequency SED.

In addition to the data taken during our 2003–2004 campaign, we have included historical X-ray measurements to indicate the degree of X-ray variability observed in this source and the historical average GeV γ-ray flux measured by the EGRET instrument on board the *Compton Gamma-Ray Observatory* from five observations between 1991 November and 1995 September (Hartman et al. 1999).

The shape of the time-averaged optical (*U*)*BVRI* spectra, together with the very steep X-ray spectral index, indicates that
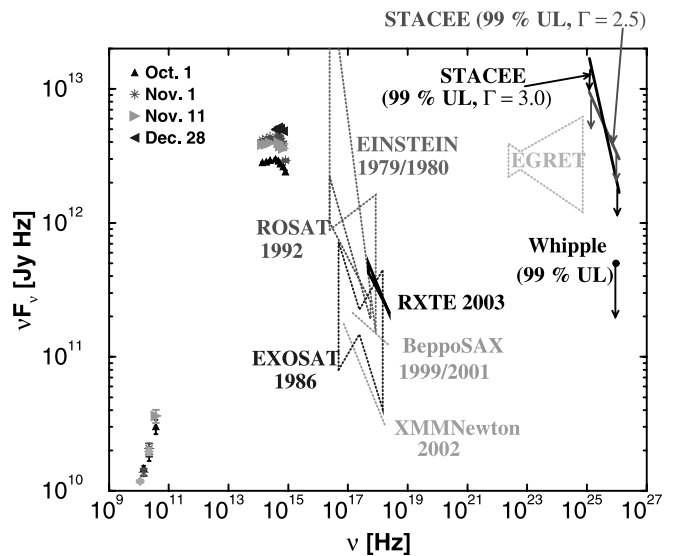

Fig. 15.—Time-averaged SEDs of 3C 66A at various epochs during the core campaign period in 2003. The turquoise diamonds indicate the average of the RATAN-600 measurements from 2003 October 11 and 14. Historical soft X-ray spectra are plotted for comparison; the hard X-ray spectrum labeled *RXTE* 2003 indicates the result of a power-law fit to the *RXTE* PCA observations of this campaign. The historical (noncontemporaneous) average of the five EGRET pointings on the source is also included for reference. All data that are not contemporaneous with our campaign are indicated by dotted curves. [*See the electronic edition of the Journal for a color version of this figure.*]

the νF_ν peak of the synchrotron component of 3C 66A is typically located in the optical range. The shape of our best-fit *RXTE* spectrum provides strong evidence that the synchrotron component extends far into the X-ray regime and intersects the high-energy component in the time-averaged SED of 3C 66A at ≳10 keV during our core campaign period. Due to the lack of simultaneous GeV γ-ray coverage and of a firm detection at >100 GeV, we cannot make a precise statement concerning the level of γ-ray emission during our campaign. However, if the historical EGRET flux is representative also for the time of our campaign, then the total energy output in the low-frequency and the high-frequency components of the SED of 3C 66A are comparable, as is typical for the class of intermediate- and low-frequency peaked BL Lac objects.

6. GENERIC PARAMETER ESTIMATES

In this section we discuss some general constraints on source parameters. We first (§ 6.1) focus on parameter estimates using the SED and optical intraday variability measurements, most relevant to the innermost portion of the jet outflow, closest to the central engine. In § 6.2 we use the results of our VLBA observations to estimate parameters of the relativistic flow on parsec scales.

6.1. *Parameters of the Inner Jet*

From the minimum variability timescale of $\Delta t_{\min} \sim 2$ hr, we can estimate the size of the emitting region as $R \lesssim cD\Delta t_{\min}$, where $D = [\Gamma(1 - \beta_\Gamma \cos\theta_{\rm obs})]^{-1}$, where Γ is the bulk Lorentz factor of the emitting region, $\beta_\Gamma c$ is the corresponding speed, and $\theta_{\rm obs}$ is the observing angle. This yields $R \lesssim 2.2 \times 10^{15}\ \delta_1$ cm, where $\delta = 10\delta_1 \sim 15$ as an estimate from the limits on superluminal motion and from previous modeling efforts, as mentioned in the introduction.

An estimate of the comoving magnetic field can be found by assuming that the dominant portion of the time-averaged

synchrotron spectrum is emitted by a quasi-equilibrium power-law spectrum of electrons with $N_e(\gamma) = n_0 V_B \gamma^{-p}$ for $\gamma_1 \leq \gamma \leq \gamma_2$; here V_B is the comoving blob volume. Based on the X-ray spectral index of $\alpha \approx 1.5$, we find a particle spectral index of $p \approx 4$. Since the synchrotron cooling timescale for X-ray–emitting electrons might be much shorter than the dynamical timescale (see eq. [3]), the X-rays are likely to be produced by a cooled electron distribution. In this case, the index $p \approx 4$ corresponds to a distribution of electrons injected into the emission region with an original index $q \approx 3$. The normalization constant n_0 is related to the magnetic field through an equipartition parameter $e_B \equiv u_B/u_e$ (in the comoving frame). Note that this equipartition parameter only refers to the energy density of the electrons, not accounting for a (possibly dominant) energy content of a hadronic matter component in the jet. Under these assumptions, the magnetic field can be estimated as described, e.g., in Böttcher et al. (2003). Taking the νF_ν peak synchrotron flux f_ϵ^{sy} at the dimensionless synchrotron peak energy ϵ_{sy} as $\sim 5 \times 10^{-11}$ ergs cm^{-2} s^{-1} at $\epsilon_{\mathrm{sy}} \approx 5 \times 10^{-6}$ and $R \approx 3.3 \times 10^{15}$ cm, we find

$$B_{e_B} = 4.4 \delta_1^{-1} e_B^{2/7} \text{ G}, \qquad (1)$$

which yields $B_{e_B} \approx 2.9 \; e_B^{2/7}$ G for $\delta = 15$.

We can further use this magnetic-field value to estimate the end points of the electron spectrum since the low-energy end, γ_1, might correspond to the νF_ν peak of the synchrotron spectrum, and the synchrotron high-energy cutoff corresponds to γ_2. Generally, we find

$$\gamma \approx 3.1 \times 10^3 \; \nu_{15}^{1/2} \left(\frac{\delta}{15}\right)^{-1/2} \left(\frac{B}{2.9 \text{ G}}\right)^{-1/2}, \qquad (2)$$

where ν_{15} is the characteristic synchrotron frequency in units of 10^{15} Hz. With our standard parameters, this yields $\gamma_1 \approx 3.1 \times 10^3$ and $\gamma_2 = 1.5 \times 10^5$ if the synchrotron cutoff occurs around 10 keV. We can also use this to estimate the synchrotron cooling timescale of electrons in the observer's frame:

$$\tau_{\mathrm{cool,sy}}^{\mathrm{obs}} \approx 2.8 \times 10^3 \left(\frac{\delta}{15}\right)^{-1/2} \left(\frac{B}{2.9 \text{ G}}\right)^{-3/2} \nu_{15}^{-1/2} \text{ s.} \qquad (3)$$

For optical frequencies, this yields observed cooling timescales of the order of ~ 2 hr, in agreement with the observed minimum variability timescale. This, however, raises an important caveat. The observed minimum variability timescale may, in fact, be a reflection of the electron cooling timescale rather than the dynamical timescale, as we had assumed when choosing our estimate for the source size R. For this reason, a more detailed future investigation of possible short-term variability at X-ray frequencies will be extremely important to resolve this issue. If X-ray variability on shorter timescales than ~ 2 hr is found, the emission region would then have to be more compact than the $R \sim 3 \times 10^{15}$ cm that we had estimated here, and X-ray spectral hysteresis patterns could arise. In contrast, if the X-ray variability timescale is found to be consistent with the optical one, then it would have to be dominated by the dynamical timescale and thus be largely achromatic. Thus, in that case no significant X-ray spectral hysteresis would be expected.

6.2. Parameters of the Parsec-Scale Outflow

In our analysis of the 22 and 43 GHz VLBA maps of 3C 66A, we had found a rather smooth jet, with only one of the six Gaussian components (C1) showing evidence for superluminal

TABLE 6
Core Brightness Temperatures and Corresponding Lower Limits, Calculated from the Measured 43 GHz VLBA Fluxes and Component Sizes

Epoch	T_b^{core} (K)	$T_{b,\mathrm{min}}^{\mathrm{core}}$ (K)
2003.78.............................	2.7×10^{11}	1.1×10^{11}
2003.83.............................	2.0×10^{11}	1.0×10^{11}
2004.08.............................	6.6×10^{11}	1.4×10^{11}

motion of $\beta_{\mathrm{app}} = (8.5 \pm 5.6) \; h^{-1}$. If we consider the measured speed of the component C1 to be close to the maximum as observed under the superluminal angle given by $\cos(\theta_{\mathrm{obs}}^{\mathrm{SL}}) = \beta_\Gamma$, we can estimate the minimum Lorentz factor and maximum angle between the jet and our line of sight. With $h = 0.7$ and by taking the lower limit of the $\beta_{\mathrm{app}} \geq (8.5-5.6) \; h^{-1} = 2.9 \; h^{-1}$, we have a lower limit to the bulk Lorentz factor of $\Gamma \geq 4.3$ and an upper limit to the viewing angle of $\theta_{\mathrm{obs}} \leq 27°2$. The large error in β_{app} results in very weak constraints on Γ and θ_{obs}, and they should be considered as very conservative estimates. Much more accurate values should be available after the analysis of all nine epochs of the VLBA monitoring program (T. Savolainen et al. 2005, in preparation).

From the measured fluxes at 22 and 43 GHz, we have calculated the brightness temperatures along the jet. The largest brightness temperatures are found for the core, yielding lower limits of $T_b^{\mathrm{core}} \sim 10^{11}$ K (see Table 6). Here we have to mention the caveat that the errors for the size of the core are very difficult to estimate, since our model-fitting yields very asymmetric probability density distributions for the core size. Essentially, the data are also consistent with a point-source core, so we can only give an upper limit to the core size. Thus, no upper limit to the core brightness temperature is available. Our calculated best-fit core brightness temperatures and corresponding lower limits are listed in Table 6 and can be compared with an equipartition brightness temperature (Readhead 1994) for 3C 66A of $T_{b,\mathrm{ep}} = 6 \times 10^{10}$ K. If the equipartition assumption holds, the minimum Doppler factor is around 2. The same result was obtained by Lähteenmäki & Valtaoja (1999), who used variability arguments to calculate the Doppler factor. Because we do not have upper limits for the brightness temperature, we cannot calculate a more precise value for the Doppler factor. However, if the core brightness temperatures calculated from the best model-fit values are not too far from the truth, the core Doppler factor probably lies somewhere between 2 and 15, with the average best-fit value of 6.

We have also calculated the brightness temperatures for components other than the core at both 22 and 43 GHz. In Figure 16 the component brightness temperatures are plotted against the component distance from the core. The figure illustrates that the points form two well-defined power laws with a different scaling at different frequencies. All three epochs are included in the plot (and coded by colors). The brightness temperature gradient along the jet is well described by a power law $T_b \propto r^s$ with $s = -2$. There is an exception to the power law between 1.8 and 2.3 mas from the core, where the brightness temperature increases above the power law fit by a factor of 3–5. This takes place in the jet region B, where the jet is clearly bending. This brightening could be a result of a temporary increase of the Doppler factor caused by the bending of the jet toward our line of sight. An alternative interpretation could be given by impulsive particle acceleration in region B by a standing shock
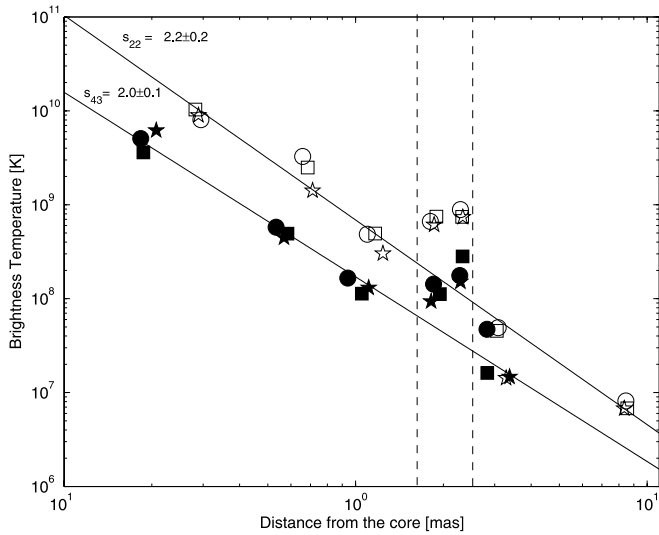
FIG. 16.—VLBA brightness temperatures as a function of distance from the core, at 22 GHz (*filled symbols*) and 43 GHz (*open symbols*), for the three epochs: 2003.78 (*circles*), 2003.83 (*squares*), and 2004.08 (*stars*). The solid lines are our best-fit power laws to the brightness-temperature profiles; the vertical dashed lines indicate the jet regions B2 and B3, where a significant deviation from the power-law profile is found, coincident with an apparent kink in the jet flow direction.

FIG. 17.—Transverse diameter D (FWHM of Gaussian component fits) of the jet as a function of distance from the core for the inner 3 mas. The symbols are the same as in Fig. 16. The solid curve illustrates the best-fit power law $D \propto r^d$, which yields $d = 0.6$.

wave caused by the interaction of the continuous, relativistic outflow with the observed kink.

The power law gradient of the brightness temperature along the jet suggests that 3C 66A exhibits a smooth parsec-scale jet without any prominent particle acceleration sites (shocks) other than the core and possibly the bend in region B. If we assume that the magnetic field B, the electron density N and the cross-sectional diameter D of the jet can also be described by the power laws $N \propto r^n$, $B \propto r^b$, and $D \propto r^d$, then the brightness temperature is expected to fall with r as $T_b \propto r^s$ (with $s < 0$). If optically thin synchrotron emission and a constant Lorentz factor of the emitting electrons are assumed, $s = d + n + b(1 + \alpha)$, where α is the spectral index (see, e.g., Kadler et al. 2004). If we know the values of s, d and α, we can calculate the relationship between b and n, or, by assuming equipartition, the actual values of b and n. We know now that $s = -2$, and the average spectral index is $\langle \alpha_{22-43} \rangle = 0.15$.

We still need to find out the value of d. The value $d = 1$ would correspond to a constant opening angle (conical jet), but our imaging results allow us to estimate a more precise value from the data by plotting the component size versus distance from the core (see Fig. 17). Surprisingly, up to 2.5 mas from the core, the jet is very tightly collimated. A power-law fit to the observed correlation between the lateral jet size and distance from the core yields $d = 0.6$. After 2.5 mas, the jet opens up (or disrupts) and d becomes larger than 1. This might be another indication that the angle between the jet and our line of sight is changing along the jet. The observed opening angle of the jet, ψ_{obs}, is related to the intrinsic opening angle ψ_{int}, through $\psi_{\mathrm{obs}} \approx \psi_{\mathrm{int}}/\sin(\theta_{\mathrm{obs}})$ for small values of ψ_{int} and θ_{obs}. Thus, the observed opening angle increases when the jet bends toward our line of sight, which is in accordance with the observed brightening of the jet in region B.

If equipartition holds, we may assume $n = 2b$. Then, taking $d = 0.6$ yields $b = -0.8$ and $n = -1.7$. For the case of a conical jet ($d = 1$), we find $n = -1.9$ and $b = -1.0$. If the equipartition assumption holds, these results mean that in a conical jet, the magnetic field decays as $B \propto D^{-1}$, and in a collimated
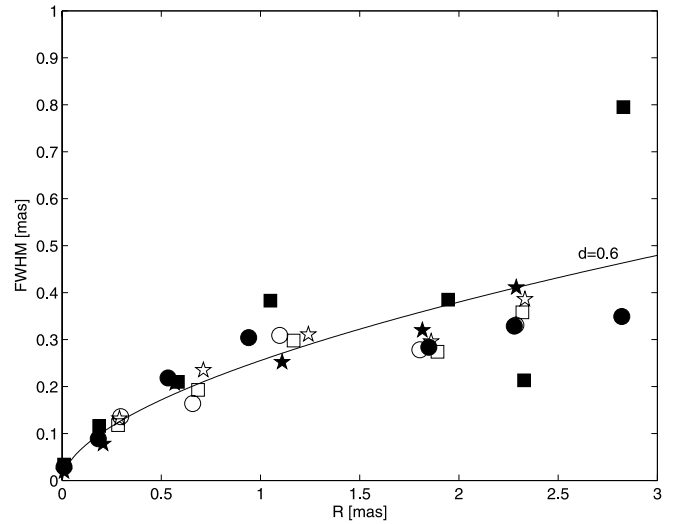
jet ($d = 0.6$), it decays as $B \propto D^{-1.3}$, implying a magnetic field that is predominantly transverse to the jet axis. This is in accordance with other observational results on the magnetic field orientation in BL Lac objects in general (see, e.g., Gabuzda et al. 2004). A magnetic field being predominantly transverse to the jet agrees well with overall toroidal field configuration, which is expected in Poynting flux dominated jet models. Another possibility for creating predominantly transverse magnetic field is the enhancement of the transverse magnetic field component by a series of shocks, but this seems to be less likely in this case, since we do not observe bright knots in the jet, but a rather smooth flow.

7. SUMMARY

We have observed 3C 66A in a massive multiwavelength monitoring campaign from 2003 July to 2004 April. Monitoring observations were carried out at radio, infrared, optical, X-ray, and VHE γ-ray observations. The main observational results of our campaign are the following:

1. In the optical, several outbursts by $\Delta m \sim 0.3$–0.5 over timescales of several days were observed.

2. Optical intraday microvariability ($\Delta m \lesssim 0.05$) on timescales of $\Delta t_{\mathrm{var}} \sim 2$ hr was detected.

3. No clear evidence for periodicity was found, but a quasi-regular sequence of several major outbursts separated by ~ 50–57 days was identified.

4. Large optical flares (on timescales of several days) seem to exhibit optical spectral hysteresis, with the $B - R$ hardness peaking several days prior to the R- and B-band flux peaks.

5. The 3–10 keV X-ray spectrum is best fitted with a single power law with energy index $\alpha = 1.47 \pm 0.56$, indicating that the transition between the synchrotron and the high-energy components occurs at photon energies of $\gtrsim 10$ keV.

6. Radio VLBA monitoring observations reveal a rather smooth jet with no clearly discernible knots or hot spots except for moderate brightening in region B, where the jet is bending.

7. Decomposition of the VLBA radio structure into Gaussian components reveals superluminal motion only for one of six

components. Its apparent speed is $\beta_{\mathrm{app}} = (8.5 \pm 5.6)\, h^{-1} = (12.1 \pm 8.0)$ for $h = 0.7$.

8. The radio brightness temperature profile along the jet, along with its observed geometry, $D \propto r^{0.6}$, suggest a magnetic field decay $B \propto D^{-1.3}$, indicating a predominantly perpendicular magnetic field orientation.

9. STACEE observations revealed a 2.2 σ excess, which provided strict upper limits at $E_\gamma \gtrsim 150$ GeV. Additional VHE γ-ray limits at $E_\gamma > 390$ GeV resulted from simultaneous Whipple observations.

10. The broadband SED of 3C 66A during our campaign suggests that the synchrotron component peaks in the optical and extends far into the X-ray regime, out to at least ~ 10 keV.

11. The following parameters of the synchrotron emission region near the core can be estimated:

$$\delta \approx 15, \tag{4}$$

$$R \approx 3.3 \times 10^{15} \text{ cm}, \tag{5}$$

$$B \approx 2.9\; \epsilon_B^{2/7} \text{ G}, \tag{6}$$

$$\gamma_1 \approx 3.1 \times 10^3, \tag{7}$$

$$\gamma_2 \approx 1.5 \times 10^5, \tag{8}$$

$$p \approx 4. \tag{9}$$

12. No X-ray variability was detectable by *RXTE* on a ~ 1 day timescale. Future X-ray observations with more sensitive X-ray detectors will be important to probe for rapid X-ray variability

and X-ray spectral hysteresis in order to put more stringent constraints on the source size, the nature of the variability mechanism, and the composition and energetics of the emitting plasma in the jet.

REFERENCES

Aharonian, F., et al. 2002, A&A, 384, L23
Aller, H. D., Aller, M. F., Latimer, G. E., & Hodge, P. E., 1985, ApJS, 59, 513
Aller, M. F., Aller, D. H., & Hughes, P. A. 1994, in Workshop on Intensive Monitoring of OJ 287, ed. M. R. Kidger & L. O. Takalo (Tuorla Obs. Rep. 174; Piikkiö: Turku Univ.), 60
Bessel, M. S., Castelli, F., & Plez, B. 1998, A&A, 337, 231
Böttcher, M. 2002, in 37th Rencontres de Moriond, 22nd Moriond Astrophysics Meeting, The Gamma-Ray Universe, ed. A. Goldwurm et al. (Hanoi: Thê Giói), 151
Böttcher, M., et al. 2003, ApJ, 596, 847
Bramel, D. A., et al. 2005, ApJ, 629, 108
Carini, M. T., & Miller, H. R. 1991, BAAS, 23, 1420
Catanese, M., et al. 1998, ApJ, 501, 616
Chadwick, P. M., et al. 1999, ApJ, 513, 161
Costamante, L., & Ghisellini, G. 2002, A&A, 384, 56
Croston, J. H., Hardcastle, M. J., Birkinshaw, M., & Worrall, D. M. 2003, MNRAS, 346, 1041
De Diego, J. A., Kidger, M. R., Gonzáles-Pérez, N., & Lehto, H. 1997, A&A, 318, 331
de Jager, O., & Stecker, F. W. 2002, ApJ, 566, 738
Edelson, R. A., & Krolik, J. H. 1988, ApJ, 333, 646
Falcone, A. D., et al. 2004, ApJ, 613, 710
Fan, J. H., & Lin, R. G. 1999, ApJS, 121, 131
———. 2000, ApJ, 537, 101
Fossati, G., Maraschi, L., Celotti, A., Comastri, A., & Ghisellini, G. 1998, MNRAS, 299, 433
Gabuzda, D. C., Eamonn, M., & Cronin, P. 2004, MNRAS, 351, L89
Ghisellini, G., Celotti, A., Fossati, G., Maraschi, L., & Comastri, A. 1998, MNRAS, 301, 451
González-Pérez, J. N., Kidger, M. R., & Martín-Luis, F. 2001, AJ, 122, 2055
Greisen, E. W. 1988, in Acquisition, Processing, and Archiving of Astronomical Images, ed. G. Longo & G. Sedmak (Napoli: Osservatorio Astronomico di Capodimonte), 125
Hartman, R. C., et al. 1999, ApJS, 123, 79
Hillas, A. M., et al. 1998, ApJ, 503, 744
Holder, J., et al. 2003, ApJ, 583, L9
Homan, D. C., Ojha, R., Wardle, J. F. C., Roberts, D. H., Aller, M. F., Aller, H. D., & Hughes, P. A. 2001, ApJ, 549, 840
Horan, D., et al. 2002, ApJ, 571, 753
———. 2004, ApJ, 603, 51

Jorstad, S. G., Marscher, A. P., Mattox, J. R., Wehrle, A. E., Bloom, S. D., & Yurchenko, A. V. 2001, ApJS, 134, 181
Jorstad, S. G., et al. 2005, ApJ, submitted (astro-ph/0502501)
Kadler, M., Ros, E., Lobanov, A. P., Falcke, H., & Zensus, J. A. 2004, A&A, 426, 481
Kovalev, Y. Y., et al. 1999, A&AS, 139, 545
Lähteenmäki, A., & Valtaoja, E. 1999, ApJ, 521, 493
Lainela, M., et al. 1999, ApJ, 521, 561
Lanzetta, K. M., Turnshek, D. A., & Sandoval, J. 1993, ApJS, 84, 109
Lovell, J. 2000, in Astrophysical Phenomena Revealed by Space VLBI, ed. H. Hirabayashi, P. G. Edwards, & D. W. Murphy (Sagamihara: ISAS), 301
Mattox, J. R., Hartman, R. C., & Reimer, O. 2001, ApJS, 135, 155
Miller, H. R., & McGimsey, B. Q. 1978, ApJ 220, 19
Miller, J. S., French, H. B., & Hawley, S. A. 1978, in Pittsburgh Conference on BL Lac Objects, ed. A. M. Wolfe (Pittsburgh: Univ. Pittsburgh), 176
Mücke, A., & Protheroe, R. J. 2001, Astropart. Phys., 15, 121
Mücke, A., Protheroe, R. J., Engel, R., Rachen, J. P., & Stanev, T. 2003, Astropart. Phys., 18, 593
Neshpor, Yu. I., Stepanyan, A. A., Kalekin, O. R., Fomin, V. P., Chalenko, N. N., & Shitov, V. G. 1998, Astron. Lett., 24, 134
Neshpor, Yu. I., Stepanyan, A. A., Kalekin, O. R., Zhogolev, N. A., Fomin, V. P., Chalenko, N. N., & Shitov, V. G. 2000, Astron. Rep., 44, 641
Perri, M., et al. 2003, A&A, 407, 453
Price, R., Gower, A. C., Hutchings, J. B., Talon, S., Duncan, D., & Ross, G. 1993, ApJS, 86, 365
Punch, M., et al. 1992, Nature, 358, 477
Quinn, J., et al. 1996, ApJ, 456, L83
Raiteri, C. M., et al. 2001, A&A, 377, 396
———. 2005, A&A, 438, 39
Readhead, A. C. S. 1994, ApJ, 426, 51
Rieger, F. M. 2004, ApJ, 615, L5
Sambruna, R. M., Barr, P., Giommi, P., Maraschi, L., Tagliaferri, G., & Treves, A. 1994, ApJS, 95, 371
Schlegel, D. J., Finkbeiner, D. P., & Davis, M. 1998, ApJ, 500, 525
Shepherd, M. C. 1997, in ASP Conf. Ser., 125, Astronomical Data Analysis Software and Systems VI, ed. G. Hunt & H. E. Payne (San Francisco: ASP), 77
Takalo, L. O., Kidger, M. R., de Diego, J. A., Sillanpää, A., & Nilsson, K. 1992, AJ, 104, 40
Takalo, L. O., et al. 1996, A&AS, 120, 313

Taylor, G. B., Vermeulen, R. C., Readhead, A. C. S., Pearson, T. J., Henstock, D. R., & Wilkinson, P. N. 1996, ApJS, 107, 37
Teräsranta, H., et al. 1998, A&AS, 132, 305
Vagnetti, F., Trevese, D., & Nesci, R. 2003, ApJ, 590, 123
Villata, M., et al. 2000, A&A, 363, 108
———. 2002, A&A, 390, 407
———. 2004a, A&A, 421, 103
———. 2004b, A&A, 424, 497
Walker, M. A. 1998, MNRAS, 294, 307

Weekes, T. C., et al. 2002, Astropart. Phys., 17, 221
Wills, B. J., & Wills, D. 1974, ApJ, 190, L97
Worrall, D. M., Puschell, J. J., Rodriguez-Espinosa, J. M., Bruhweiler, F. C., Miller, H. R., Aller, M. F., & Aller, H. D. 1984, ApJ, 286, 711
Worrall, D. M., & Wilkes, B. J. 1990, ApJ, 360, 396
Wurtz, R., Stocke, J. T., & Yee, H. K. C. 1996, ApJS, 103, 109
Xie, G. Z., Li, K. H., Liu, F. K., Wu, J. X., Fan, J. H., Zhu, Y. Y., & Cheng, F. Z. 1992, ApJS, 80, 683